PROTEUS: A Coupled Iterative Force-Correction Immersed-Boundary Cascaded Lattice Boltzmann Solver for Moving and Deformable Boundary Applications

PROTEUS: A Coupled Iterative Force-Correction Immersed-Boundary Cascaded Lattice Boltzmann Solver for Moving and Deformable Boundary Applications.

E. J. Falagkaris[a,*], D. M. Ingram[a], K. Markakis[a], I. M. Viola[a]

[a]*Institute of Energy Systems, School of Engineering, The University of Edinburgh, Colin Maclaurin Rd, EH9 3DW, Edinburgh, UK*

Abstract

Many realistic fluid flow problems are characterised by high Reynolds numbers and complex moving or deformable geometries. In our previous study, we presented a novel coupling between an iterative force-correction immersed boundary and a multi-domain cascaded lattice Boltzmann method, Falagkaris *et al.*, and investigated flows around rigid bodies at Reynolds numbers up to 10^5. Here, we extend its application to flows around moving and deformable bodies with prescribed motions. Emphasis is given on the influence of the internal mass on the computation of the aerodynamic forces including deforming boundary applications where the rigid body approximation is no longer valid. Both the rigid body and the internal Lagrangian points approximations are examined. The resulting solver has been applied to viscous flows around an in-line oscillating cylinder, a pitching foil, a plunging SD7003 airfoil and a plunging and flapping NACA-0014 airfoil. Good agreement with experimental results and other numerical schemes has been obtained. It is shown that the internal Lagrangian points approximation accurately captures the internal mass effects in linear and angular motions, as well as in deforming motions, at Reynolds numbers up to $4 \cdot 10^4$. In all cases, the aerodynamic loads are significantly affected by the internal fluid forces.

Keywords: Cascaded lattice Boltzmann method, Immersed boundary method, Iterative force-correction, Moving and deformable geometries, Internal mass effects

1. Introduction

One of the challenging and important issues in computational fluid dynamics (CFD) is the accurate and efficient treatment of complex moving or deformable boundaries. This study will focus on the effect of the internal mass on the aerodynamic forces acting on a moving body, using a coupled immersed boundary cascaded lattice Boltzmann solver.

The lattice Boltzmann method (LBM) has been developed into a promising numerical scheme for simulating viscous fluid flows and has been successfully applied on both rigid and moving boundary applications. The consistency of the LBM with regard to the Navier-Stokes equations (NSE) has been established through various methods in the literature [1, 2, 3, 4, 5, 6, 7, 8] and has been applied to many moving boundary simulations [9, 10] because of its computational efficiency, simplicity and scalable parallel nature. In this work, the cascaded lattice Boltzmann method (CLBM), recently introduced by Geier *et al.*, [11, 12], is used for the fluid flow simulation due to its superior stability properties and higher degree of Galilean invariance over other lattice Boltzmann schemes [13, 14, 15, 16, 17, 18].

In most practical fluid flow problems involving complex moving or deformable boundaries, non-uniform grid or body-fitted methods have been commonly used in the literature. Such treatments however, involve complicated algorithms with high computational costs and the solution accuracy is not as high as in uniform grid solvers. Decoupling the solution of the governing fluid equations from the implementation of the boundary conditions can simplify the solution process. The immersed boundary method (IBM), which was introduced by Peskin [19] in the 1970s to simulate blood flows in the human heart, has recently received great attention in simulating flows with complex moving geometries on a fixed Cartesian grid [20, 21, 22, 23].

*Corresponding Author. Tel.: +44 7469 895975
Email address: E.falagkaris@ed.ac.uk (E. J. Falagkaris)

In IBM, the physical boundary is represented by a set of Lagrangian points, independent of the fixed Cartesian grid points. The no-slip condition on the boundary is enforced by applying body forces near the boundary resulting in movement of the internal to the body fluid. The motion of the internal fluid does not affect the flow characteristics outside the boundary. However, as pointed out by Suzuki and Inamuro [24], if the forces acting on the boundary are obtained by the negative sum of the body forces, as in [25], they are influenced by the motion of the internal mass. There have been only a few studies on the effect of the internal mass on the computation of the aerodynamic forces [26, 27, 28]. Uhlmann [27] treated the internal mass as a rigid body, imposing, however, a limitation on the density ratio of the body to the fluid for a stable simulation. Uhlmann [27] also computed the effect of the internal mass by summing the forces over all internal Eulerian points. However, the identification of the internal Eulerian points in a moving boundary application is very complex and computationally expensive. A similar observation on the limitation of the density ratio of the body to the fluid has been made by Ladd and Verberg [29]. Feng and Michaelides [28] further developed the work of Uhlmann [27] by eliminating the limitation on the density ratio. Shen *et al.* [30], following the work of Balaras [31], investigated the effect of the internal mass by integrating the NSE with the body forces. The magnitude of the internal mass effects was examined in systems with prescribed boundary motions. Most recently, Suzuki and Inamuro [24] proposed the Lagrangian point approximation (LPA) as an efficient method for describing the internal mass effects and compared it with the previous methods of Uhlmann [27] and Feng and Michaelides [28]. They examined the effect of the internal mass in cases where the body motion is defined by the fluid flow as well as, the dependency of the effect on very low Reynolds number flows. In the present study, the Lagrangian point approximation of Suzuki and Inamuro [24] is used. We focus on identifying the optimal configuration between arrangement of Lagrangian points and computational efficiency, as well as on examining the accuracy of the method at high Reynolds number flows around deformable boundaries for the first time.

In recent years, many efforts have been made in order to improve the coupling between the IBM and the LBM. In the penalty method, proposed by Feng and Michaelides [9], the immersed boundary is allowed to deform slightly and is restored back to its target position using a linear spring approximation. Dupuis *et al.* [32] presented a direct-forcing IBM, where the boundary force is computed using the interpolated velocity and a desired reference velocity. The momentum exchange of the particle distributions at the boundary was used by Niu *et al.* [33] to calculate the force acting on the immersed boundary. However, the non-slip boundary condition cannot be satisfied exactly by those methods. A few iterative IB schemes exist in the literature [34, 35] that improve the accuracy of the prescribed boundary conditions. Zhang *et al.* [36] proposed an iterative force correction scheme based on Cheng's external forcing term [37]. Wu and Shu [38] developed an implicit velocity correction-based IB-LBM based on Guo's external forcing term [39]. In the present study, the iterative force correction IB scheme proposed by Zhang *et al.* [36] is used as described in our previous study [40].

This paper focuses on the effect of the internal mass in the computation of the aerodynamic forces for viscous fluid flows around moving and deformable boundaries at a wide range of Reynolds numbers. The coupled iterative direct forcing immersed boundary cascaded lattice Boltzmann method (IDF-CLBM), presented in our previous study [40], is used for the viscous fluid flow simulations. The effect of the internal mass is investigated using the Lagrangian point approximation method. First, the effect on the drag force is examined by considering the flow around a bluff body (circular cylinder) oscillating in a stationary fluid. Second, the effect on the lift force is examined by investigating the flow around streamlined bodies (foils) undergoing pitching and heaving motions. Finally, the effect on both the lift and drag forces of a plunging and deformable foil is investigated. The paper is organised as follows. In section 2, the numerical method is presented. That includes the central moment formulation of the LBM, the iterative direct forcing IBM and the LPA treatment of the internal mass. Numerical results and the accuracy and robustness of the proposed scheme are reported in Section 3. Finally, the conclusions are summarised in Section 4.

2. Numerical Method

2.1. The Cascaded lattice Boltzmann method

2.1.1. Central-moment lattice Boltzmann formulation

Consider a two-dimensional athermal fluid at a Cartesian coordinate system (x, y) and let only the density $\rho(x, y)$, the velocity $\mathbf{u} = (u_x, u_y)$, and the external forces $\mathbf{F}(x, y)$ to characterize its local hydrodynamic behaviour. The nine-velocity square lattice model, denoted as D2Q9 [14], has been successfully used in the literature [41] for two-dimensional flows. Under the presence of external forces, the discrete evolution equation for the CLBM may

be written as

$$f_\alpha(\mathbf{x}+\mathbf{e}_\alpha\delta t, t+\delta t) = f_\alpha(\mathbf{x},t) + \Omega_a(\mathbf{x},t) + \delta t S_a, \tag{1}$$

where $\mathbf{e}_\alpha : \alpha = 0,1,\ldots,8$ is the discrete velocity set; $f_\alpha(\mathbf{x},t) : \alpha = 0,1,\ldots,8$ are the discrete particle distribution functions (PDF) at time t and position $\mathbf{x}$; $\Omega_\alpha(\mathbf{x},t) : \alpha = 0,1,\ldots,8$ is the discrete collision operator, and $S_\alpha(\mathbf{x},t) : \alpha = 0,1,\ldots,8$ are the discrete forcing terms. Using the transformation matrix $\mathbf{K}$ [42, 12] the collision operator takes the form $\mathbf{\Omega}_a = (\mathbf{K}\cdot\hat{\mathbf{k}})_a$, where $\hat{\mathbf{k}} = \hat{k}_a(\mathbf{x},t) : \alpha = 0,1,\ldots,8$ are the moments of the distribution functions. The general expression of the collision kernel without integrated force terms is of the form

$$\hat{k}_0 = \hat{k}_1 = \hat{k}_2 = 0, \tag{2}$$

$$\hat{k}_3 = \omega_3\frac{1}{12}\Big\{-(f_1+f_2+f_3+f_4+2(f_5+f_6+f_7+f_8)) + \frac{2}{3}\rho + \rho(u_x^2+u_y^2)\Big\}, \tag{3}$$

$$\hat{k}_4 = \omega_4\frac{1}{4}\Big\{(f_2+f_4-f_1-f_3) + \rho(u_x^2-u_y^2)\Big\}, \tag{4}$$

$$\hat{k}_5 = \omega_5\frac{1}{4}\Big\{(f_5+f_7-f_6-f_8) - \rho u_x u_y\Big\}, \tag{5}$$

$$\begin{aligned}\hat{k}_6 = \omega_6\frac{1}{4}\Big\{&(f_5+f_6-f_7-f_8-2u_x(f_5+f_7-f_6-f_8)-u_y(f_1+f_3+f_5+f_6+f_7+f_8))\\ &+2\rho u_x^2 u_y\Big\} - 2u_x\hat{k}_5 - \frac{1}{2}u_y(3\hat{k}_3+\hat{k}_4),\end{aligned} \tag{6}$$

$$\begin{aligned}\hat{k}_7 = \omega_7\frac{1}{4}\Big\{&(f_5+f_8-f_6-f_7-2u_y(f_5+f_7-f_6-f_8)-u_x(f_2+f_4+f_5+f_6+f_7+f_8))\\ &+2\rho u_x u_y^2\Big\} - 2u_y\hat{k}_5 - \frac{1}{2}u_y(3\hat{k}_3+\hat{k}_4),\end{aligned} \tag{7}$$

$$\begin{aligned}\hat{k}_8 = \omega_8\frac{1}{4}\Big\{&-(f_5+f_6+f_7+f_8-2u_x(f_5+f_8-f_6-f_7)-2u_y(f_5+f_6-f_7-f_8)\\ &+u_x^2(f_2+f_4+f_5+f_6+f_7+f_8)+u_y^2(f_1+f_3+f_5+f_6+f_7+f_8)+4u_xu_y(f_5+f_7-f_6-f_8))\\ &+\frac{1}{9}\rho+3\rho u_x^2u_y^2\Big\} - 2\hat{k}_3 - \frac{1}{2}u_x^2(3\hat{k}_3-\hat{k}_4) - \frac{1}{2}u_y^2(3\hat{k}_3+\hat{k}_4) - 4u_xu_y\hat{k}_5 - 2u_y\hat{k}_6 - 2u_x\hat{k}_7,\end{aligned} \tag{8}$$

where $\omega_\alpha : \alpha = 3,4,\ldots,8$ are the relaxation parameters for the different moments. Under the requirement of maintaining an isotropic stress tensor, it occurs that $\omega_4 = \omega_5$. Using the Chapman-Enskog multiscale analysis, ω_4 and ω_5 determine the kinematic shear viscosity of the fluid as $\nu = c_s^2\big({\omega_{(4,5)}}^{-1} - 0.5\big)$, where $c_s = 1/\sqrt{3}$ is the speed of sound for the D2Q9 model. Following Geier for a stable numerical approach, higher-order moments are equilibrated, i.e. $\omega_6 = \omega_7 = \omega_8 = 1$. Finally, the hydrodynamic variables, fluid density and velocity, are obtained by taking the zeroth and first moments of the distributions as

$$\rho = \sum_\alpha^q f_\alpha = \langle f_\alpha|\rho_0\rangle, \qquad \rho u_i = \sum_\alpha^q f_\alpha e_{\alpha i} = \langle f_\alpha|e_{\alpha i}\rangle, \quad i \in x,y, \tag{9}$$

where $|\rho_0\rangle = (1,1,1,1,1,1,1,1,1)^\dagger$ is the density basis vector and the superscript $\dagger$ is the transpose operator.

2.1.2. Cheng's formulation of the discrete external force term

In order to incorporate both space and time effects in the external forces, the discrete forcing term S_α in Eq. (1) is described as

$$S_\alpha = 0.5[s_\alpha(\mathbf{x}+\mathbf{e}_\alpha\delta t, t+\delta t) + s_\alpha(\mathbf{x},t)], \tag{10}$$

$$s_\alpha = w_\alpha\big\{A + 3\mathbf{B}\cdot[(\mathbf{e}_\alpha-\mathbf{u}) + 3(\mathbf{e}_\alpha\cdot\mathbf{u})\mathbf{e}_\alpha]\big\}. \tag{11}$$

Following Cheng and Li [37], we take $A = 0$ and $\mathbf{B} = \mathbf{F} = (F_x, F_y)$. Eqs. (10 - 11) are used in the iterative immersed boundary treatment as described in 2.3.

2.2. The Immersed bounary method - Iterative direct forcing formulation

Consider a closed curve $\mathscr{C}(t)$ immersed in a two-dimensional fluid domain $\Omega(t)$. The governing equations of the immersed boundary formulation for viscous incompressible flows can be found in Appendix A. In this study, the smoothed 4-point delta function [43], $\phi_4^*(r)$, will be used for the force spreading in Eq. (A.3) and the Lagrange polynomials for the velocity interpolation, $U_{l(\mathbf{X}_l,t)}$, in Eq. (A.4) as

$$\phi_4^*(r) = \begin{cases} \frac{3}{8} + \frac{\pi}{32} - \frac{r^2}{4} & \text{if } |r| \leq 0.5 \\ \frac{1}{4} + \frac{1-|r|}{8}\sqrt{-2+8|r|-4r^2} - \frac{1}{8}\arcsin(\sqrt{2}(|r|-1)) & \text{if } 0.5 \leq |r| \leq 1.5 \\ \frac{17}{16} - \frac{\pi}{64} - \frac{3|r|}{4} + \frac{r^2}{8} + \frac{|r|-2}{16}\sqrt{-14+16|r|-4r^2} & \text{if } 1.5 \leq |r| \leq 2.5 \\ 0 & \text{if } 2.5 \leq |r| \end{cases}, \tag{12}$$

$$U_{l(\mathbf{X}_l,t)} = \sum_{ij}\left(\prod_{m=1,m\neq i}^{i_{max}} \frac{X_l - x_{mj}}{x_{ij} - x_{mj}}\right)\left(\prod_{n=1,n\neq j}^{j_{max}} \frac{Y_l - y_{in}}{y_{ij} - y_{in}}\right) u_{ij}(\mathbf{x} + \mathbf{e}_a\delta t, t + \delta t), \quad l = \mathscr{L}, \tag{13}$$

where X_l, Y_l are the coordinates of the Lagrangian points. This selection is based upon the observations of Zhang *et al.* [36] and Cheng *et al.* [44]. The iterative force correction IB scheme proposed by Zhang *et al.* [36] is coupled with the CLBM. A few iterative IB schemes exist in the literature [34, 35], where the velocity term in Eq. (9) is explicitly modified in order to account for the presence of external forces. Therefore, as shown in our previous study [40], the overall accuracy of the surrounding flow field rather deteriorates as the number of iterations in the IBM increases. A similar result has been reported by Kang [34].

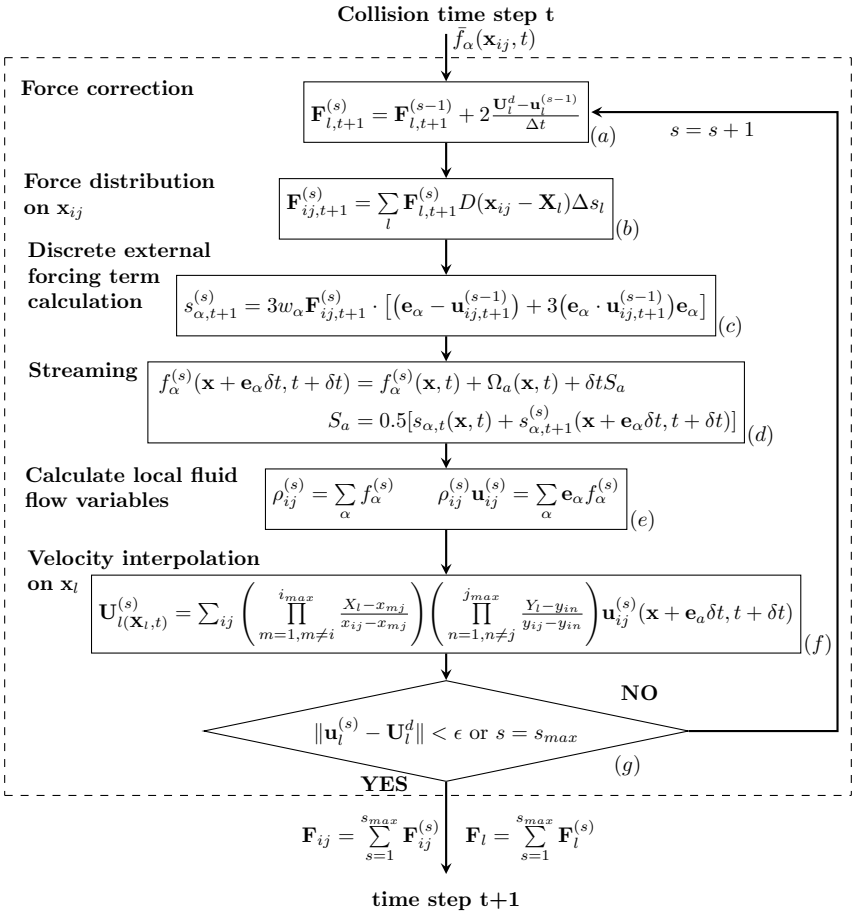

Figure 1: Computational algorithm of the iterative force correction IBM

A different approach is used in the present work. Following Cheng and Li's approach [37], in order to integrate the force effects of both the current and the next time step, the external forcing term in Eq. (1) is split into two

parts as shown in Eq. (10). Instead of using an implicit method for the solution of Eq. (10), an iterative scheme is proposed where no modification of the velocity term in Eq.(9) is necessary. For the analytical derivation of this scheme the reader should refer to [36, 37]. The computational algorithm for the iterative force correction IB algorithm of Zhang *et al.* [36] used in this work is shown in Fig. 1.

2.3. Internal mass treatment

The effect of the internal mass in the computation of the aerodynamic forces using the IDF immersed boundary method for a moving body is investigated in this section. Only cases with prescribed boundary motions are considered. The force acting on the immersed body $\mathbf{F}_{tot}$, at time t, can be calculated by the negative sum of the computed Lagrangian forces $\mathbf{F}_l$ as

$$\mathbf{F}_{tot}(t) = -\sum_{l} \mathbf{F}_l(t)\Delta s_l, \tag{14}$$

where Δs_l is the discretisation length of the immersed surface and should be equal for all Lagrangian points l. However, the immersed body receives forces from both the external and the internal fluid, $\mathbf{F}_{IB}$ and $\mathbf{F}_{int}$ respectively. Hence, in order to accurately compute $\mathbf{F}_{IB}$, the total forces $\mathbf{F}_{tot}$ acting on the body must be compensated with the internal forces $\mathbf{F}_{int}$ used to move the internal fluid [24, 26, 27] as $\mathbf{F}_{IB}(t) = \mathbf{F}_{tot} + \mathbf{F}_{int}$. The internal forcing term $\mathbf{F}_{int}$, is given by the time derivative of the linear momentum of the internal fluid [24] as

$$\mathbf{F}_{int}(t) = \rho_f \frac{d}{dt} \int_{\mathbf{x}\in\Omega(t)} \mathbf{u}(\mathbf{x}, t) d\mathbf{x}, \tag{15}$$

where ρ_f is the fluid density. The two following schemes will be investigated for the computation of the internal forces.

2.3.1. Rigid body approximation

Assuming a rigid body motion inside the enclosed area $\Omega(t)$, following the work of Feng [28], the integral in Eq. (15) can by approximated as $\int_{\mathbf{x}\in\Omega(t)} \mathbf{u}(\mathbf{x}, t) d\mathbf{x} = V_b \mathbf{U}_b^p(\mathbf{x}, t)$, where $\mathbf{U}_b^p(\mathbf{x}, t)$ is the velocity of the internal fluid which satisfies the rigid body motion at all $\mathbf{x} = (x, y) \in \Omega$ and $V_b = M_b/\rho_b$ is the volume of the body. M_b and ρ_b are the mass and density of the rigid body respectively. According to Suzuki *et al.* [24], the equality is theoretically realised since the linear motion of the rigid body is exactly equal to that of the internal mass in spite of actual internal flows. Therefore, the time derivative of the linear momentum of the internal fluid can be approximated as

$$\frac{d}{dt} \int_{\mathbf{x}\in\Omega(t)} \mathbf{u}(\mathbf{x}, t) d\mathbf{x} \approx \frac{M_b}{\rho_b} \frac{\mathbf{U}_b^p(t) - \mathbf{U}_b^p(t - \Delta t)}{\Delta t}, \tag{16}$$

where $\mathbf{U}_b^p(t)$ is the prescribed body velocity at time t. The approximation is first order accurate in time.

2.3.2. Lagrangian points approximation

Recently, Suzuki *et al.* approximated the internal forces using internal Lagrangian points moving together with the boundary [24]. A similar approach is used here, focusing more on the identification of the optimum number as well as the distribution of the internal Lagrangian points, in order to optimise both the computational efficiency and the accuracy of the simulation.

1. Compute the surface area A_Ω of the enclosed domain $\Omega(t)$ and equally distribute N_{int} internal Lagrangian points with volume $\Delta V_{int} = 1.0$. N_{int} is the integer value of A_Ω.
2. Interpolate the velocity $\mathbf{U}_{(\mathbf{X}_{int}, t)}$ on all internal points using Eq. (13).
3. Compute the linear momentum using

$$\mathbf{P}(\mathbf{X}_{int}, t) = \Big[\sum_{\mathbf{X}_{int}(t)} \mathbf{U}_{(\mathbf{X}_{int}, t)} \Delta V_{int} \Big] S_c. \tag{17}$$

4. Approximate the internal forces using

$$\mathbf{F}_{int}(t) \approx \Big[\frac{\mathbf{P}(\mathbf{X}_{int},t)-\mathbf{P}(\mathbf{X}_{int},t-\Delta t)}{\Delta t}\Big]S_c. \tag{18}$$

S_c is a scaling factor defined as $S_c = A_\Omega/N_{int}$. Therefore, if half of the internal Lagrangian points are equally distributed for the computation of Eqs. (17-18), $N_{int} = A_\Omega/2$, then both equations must be multiplied by $S_c = 2$. All internal Lagrangian points follow the prescribed motion of the boundary thus the computational overhead is mainly caused by the interpolation step. This approach differs from the work of Uhlmann [27] where $\mathbf{P}(\mathbf{X}_{int},t)$ is approximated by summing over internal Eulerian grid points. However, in moving or deformable boundary applications the identification of the internal Eulerian grid points in every time step is computationally complex and expensive.

2.4. Multi-domain algorithm and domain boundary conditions

In the present study, the multi-domain algorithm of Lagrava *et al.* [45] is used under some minor modifications as presented in our previous study [40]. The computational multi-domain algorithm is summarized in Appendix C. It is worth noting that the fine grid scales that can not be resolved by the coarse grid are removed using a filtering operator. For more details, as well as alternative algorithms the reader should refer to [45, 46, 47, 48, 49]. The overlapping between a fine and a coarse grid is illustrated in Fig. 2a.

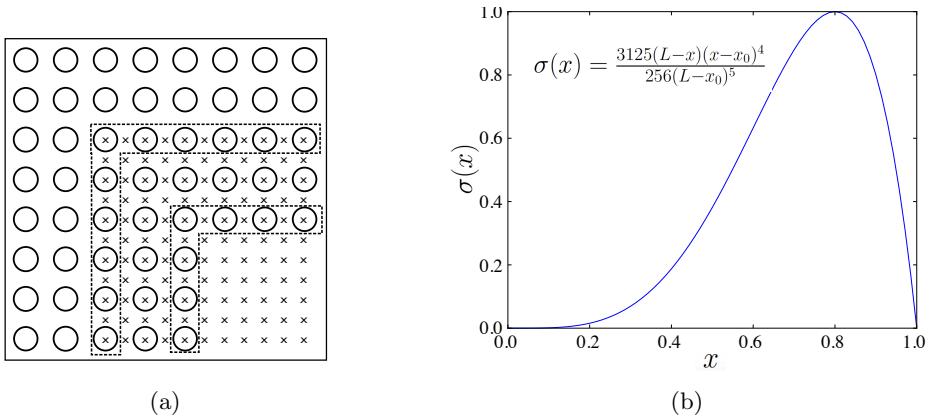

(a) (b)

Figure 2: (a): Overlapping region between fine and coarse grids. The dot enclosed areas indicate the exchange of information interfaces between two consecutive grid levels. (b): Normalized absorbing strength profile $\sigma(x)$ with $x_0 = 0$ and $L = 1$.

Unless otherwise specified, a square computational domain $100c \times 100c$, where c is the characteristic length of the immersed body, is used in this study. Following the regularization procedure of Latt and Chopard [50], all particle distributions are reconstructed at the inlet as

$$\hat{f}_\alpha = f_\alpha^{eq}(\rho,\mathbf{u}) + \frac{t_\alpha}{2c_s^4}\mathbf{Q}_\alpha : \mathbf{\Pi}^{(neq)}, \tag{19}$$

where the tensors $\mathbf{Q}_\alpha$ and $\mathbf{\Pi}^{(neq)}$ are defined as $\mathbf{Q}_\alpha = \mathbf{e}_\alpha\mathbf{e}_\alpha - c_s^2\mathbf{I}$ and $\mathbf{\Pi}^{(neq)} = \sum_{\alpha=0}^{q-1}\mathbf{e}_\alpha\mathbf{e}_\alpha(f_\alpha - f_\alpha^{eq})$. $\mathbf{I}$ is the identity matrix. The bounce back of off-equilibrium parts rule $f_\alpha^{(neq)} = f_{opp(\alpha)}^{(neq)}$ [51] is used for the computation of the unknown populations in the tensor $\mathbf{\Pi}^{(neq)}$. Assuming only waves normal to the boundary [52], the missing distributions at the outlet are computed using the following extrapolation scheme

$$f_\alpha(\mathbf{x},t) = f_\alpha(\mathbf{x}-\delta x, t-\delta t)\big(c_s - \mathbf{u}(\mathbf{x},t-\delta t)\delta t/\delta x + \Big(1 - \big(c_s - \mathbf{u}(\mathbf{x},t-\delta t)\big)\Big)f_\alpha(\mathbf{x},t-\delta t). \tag{20}$$

Slip boundary conditions are used for the top and bottom sides of the domain. Following the work of Xu and Sagaut [53], absorbing layers are used in all domain boundaries, in order to damp and minimize the reflection of the acoustic waves, as shown in Fig. 2b. The right hand side of Eq. (1) needs to be modified according to

$$f_\alpha(\mathbf{x}+\mathbf{e}_\alpha\delta t, t+\delta t) = f_\alpha(\mathbf{x},t) + \Omega_a^*(\mathbf{x},t) + \delta t S_a + \delta t H_\alpha^{eq}(\rho^f,\mathbf{u}^f,\rho^*,\mathbf{u}^*,t), \tag{21}$$

where $H_\alpha^{eq}(\rho^f, \mathbf{u}^f, \rho^*, \mathbf{u}^*, t) = \chi\Big(f_\alpha^{eq}(\rho^f, \mathbf{u}^f, t) - f_\alpha^{eq}(\rho^*, \mathbf{u}^*, t)\Big)$ with $\chi = \sigma(x)$ being the strength of the absorbing layer, Fig. 2b. The superscript f denotes the farfield values of the velocity and density, whereas the superscript $*$ denotes the parametrized density $\rho^* = \sum_\alpha f_\alpha + n\delta t \sum_\alpha H_\alpha^{eq}(\rho^f, \mathbf{u}^f, \rho, \mathbf{u}, t)$ and velocity $\rho^* u_j^* = \sum_\alpha e_{\alpha j} f_\alpha + m\delta t \sum_\alpha e_{\alpha j} H_\alpha^{eq}(\rho^f, \mathbf{u}^f, \rho, \mathbf{u}, t)$ [39]. $m = n = 1/2$ as in [53].

3. Results

3.1. Numerical test of overall accuracy

In order to evaluate the accuracy of the proposed IDF-CLBM coupling scheme, the two-dimensional unsteady and fully periodic Taylor-Green vortex flow in a square box is investigated. A circle with diameter $D = 0.5L$ is immersed at the center of square domain $L \times L$. The analytical solutions for the velocity and pressure are of the form:

$$\mathbf{u}(\mathbf{x}, t) = U_0 \left\{ \begin{array}{c} -\sqrt{k_y/k_x}\cos(k_x x)\sin(k_y y) \\ \sqrt{k_y/k_x}\sin(k_x x)\cos(k_y y) \end{array} \right\} e^{-t/t_d}, \tag{22}$$

$$p(\mathbf{x}, t) = p_0 - \rho U_0^2/4\big[k_y/k_x\cos(2k_x x) + k_x/k_y\cos(2k_y y)\big]e^{-2t/t_d}, \tag{23}$$

where U_0 is the initial velocity, $k_x = k_y = 2\pi/L$ are the wave vector $\mathbf{k}$ components and $t_d = [\nu(k_x^2 + k_y^2)]^{-1}$ is the decay time of the vortex. The flow field is initialised using Eqs. (22-23). Eq. (22) is used for prescribing the velocity on the immersed circle. The global error of the velocities is evaluated at time $t^* = tD/U_\infty = 1$ using the following L_2 norm error:

$$L_2^{error} \equiv \sqrt{\Big(\sum (u_x^c - u_x^a)^2 + (u_y^c - u_y^a)^2\Big)/N}, \tag{24}$$

where the summation is over the total number of grid nodes N and the superscripts, a and c, refer to the analytical and computational values respectively.

We investigate the convergence rate of the present scheme for two cases. For the definition of the apparent order of convergence the formula $p = \ln\big((L_2^{i+1} - L_2^i)/(L_2^i - L_2^{i-1})\big)/\ln(r)$ and a constant grid refinement ratio $r = 2$ are used. The superscripts in the L_2 terms denote the refinement levels ($D = 10, 20, 40, 80$). In case 1, the Reynolds number is set to $Re = U_0 D/\nu = 10$ and the relaxation time is set to be $\tau = 0.65$ as in [38]. Fig. 3a shows the global L_2-error versus the number of grid points along the cylinder. It is shown that the global second order accuracy of the CLBM is not significantly affected by the IBM. The apparent order of convergence is $p = 1.992$ for the CLBM, $p = 1.998$ for the BGK-LBM, $p = 1.986$ for the IDF-CLBM between the refining region ($D = 20 - 80$) and $p = 1.958$ for the IDF-CLBM between the refining region ($D = 10 - 40$). The L_2-error is slightly lower for the BGK LBM and in agreement with the values reported in [34]. Wu and Shu [38] reported a convergence rate of 1.9 and Kang and Hassan [34] a convergence rate of 1.98. Fig. 3b shows that as the fluid viscosity and the Mach number, $Ma = U_0/c_s$, decrease ($\tau = 0.95, 0.65, 0.56$) the magnitude of the error L_2-decreases while the convergence rate is not affected. The convergence rate of the L_2-error with respect to the Mach number is first order ($p \approx 1$) , as shown in Fig. 3c. In case 2, the flow at $Re = 10, 20, 40$ is investigated. The fluid velocity U_0 is kept constant for $Re = 10, 20, 40$ and the relaxation parameter is set to $\tau = 0.65, 0.575, 0.5375$. Fig. 3d shows that the overall accuracy of the method is not affected by the relaxation parameter. However, as the fluid viscosity decreases, a small increase in the magnitude of the L_2-error is observed.

3.2. Oscillating circular cylinder in a stationary fluid

First, the flow around an oscillating circular cylinder in a stationary fluid is considered. Dütch *et al.* [54] studied this problem both experimentally and numerically, and other numerical results have been reported in various studies [30, 55, 56, 57]. The computational domain is $100D \times 100D$, where $D = 100lu$ is the diameter of the cylinder and $lu = 1.0$ is the lattice unit. The cylinder is placed at the center of the domain and the prescribed oscillating motion is described as

$$X_c(t) = A_m \sin(2\pi f t), \tag{25}$$

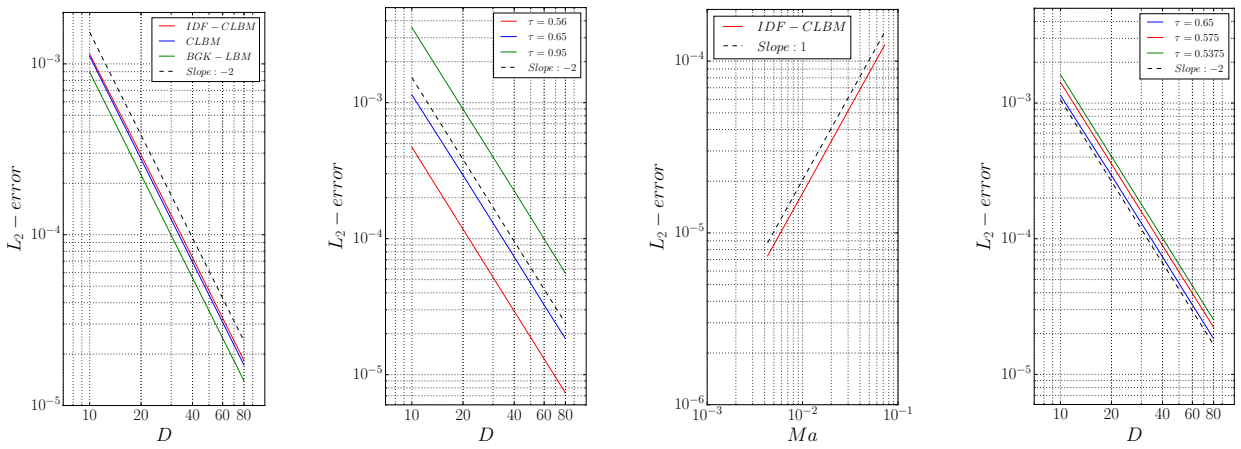

Figure 3: (a) Overall accuracy of the IDF-CLBM scheme. (b) Effect of the relaxation parameter on the overall accuracy for $Re = 10$. (c) Effect of the Mach number on the overall accuracy for $Re = 10$. (d) Effect of the relaxation parameter on the overall accuracy for constant fluid velocity and $Re = 10, 20, 40$.

where A_m denotes the amplitude and f is the characteristic frequency of the oscillating motion, as shown in Fig. 4. The non-dimensional angle of the periodic motion is ϕ, where $0 \leq \phi \leq 1$. The governing parameters of the flow are the Reynolds number $Re = U_{max}D/\nu$ and the Keulegan-Carpenter number $KC = U_{max}/fD$. The amplitude of the velocity, U_{max}, is derived from Eq. (25) as $U_{max} = 2\pi f A_m$. Thus the Keulegan-Carpenter number can be expressed as $KC = 2\pi A_m/D$. We investigate the flow at $Re = 100$ and $KC = 5$. $N_{iter} = 20$ iterations are used in the IBM algorithm.

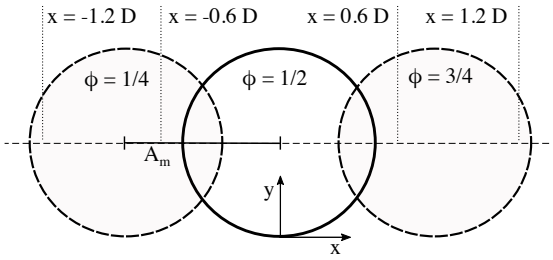

Figure 4: Schematic view of the cylinder and the oscillating motion.

The velocity profile at four cross sections ($x = x_1 - 0.6D, x_1 + 0.0D, x_1 + 0.6D, x_1 + 1.2D$) with constant $x_1 = L_x/2$ values, where L_x is the size of the domain in the x direction, and three phase angles ($\phi = 180^o, 210^o, 330^o$) are shown in Fig. 5. The experimental results of Dütch *et al.* [54] are used for comparison. Good agreement between the present results and the experimental data is observed. The symmetric and periodic vortex shedding, as well as the two-dimensional behaviour of the flow for the present parameter set up ($Re = 100$ and $KC = 5$) are well captured by the present numerical scheme. Fig. 6 shows a histogram of the interpolated velocities inside the cylinder. The mean interpolated velocity is similar to the prescribed velocity. However, as shown in Fig. 6b the highest deviations from the prescribed velocity are located near the boundary due to the force spreading kernel in the IBM. The drag coefficient $C_D = 2F_D/\rho U_{max}^2 D$ over one period of oscillation, T, is shown in Fig. 7a. The drag force F_D is computed using Eq. (14). Both the RBA and the LPA schemes are in good quantitative agreement with the computational results of Dütch *et al.* [54]. However, ignoring the internal mass effects lead to a significant over-prediction of the drag coefficient by approximately 51%, as well as to an important phase difference of 12.1^o. Fig. 7b shows the instantaneous vorticity, ω, at four phase angles, $\phi = 150^o, 180^o, 210^o, 330^o$.

Using the semi-empirical Morison equation [58], the time-dependent in-line force F_x can be predicted as

$$F_x(t) = -\frac{1}{2}\rho D C_d \dot{X}_c|\dot{X}_c| - \frac{1}{4}\pi\rho D^2 C_i \ddot{X}_c, \tag{26}$$

where C_i is the added-mass coefficient and the dots indicate the time derivatives of Eq. (25). Therefore, the

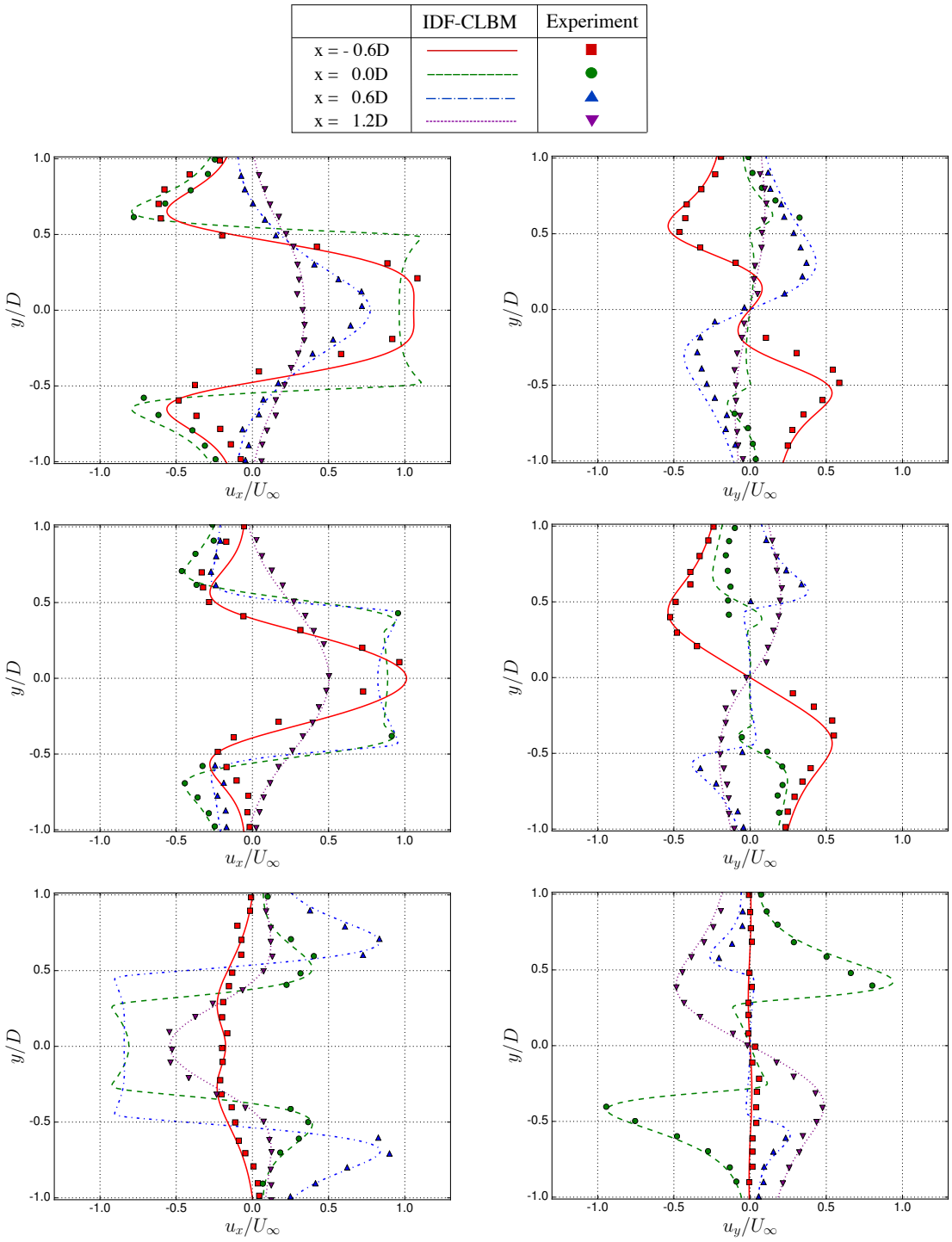

Figure 5: Velocity profiles for three phase angles (a) $\phi = 0.5$, (b) $\phi = 0.58$ and (c) $\phi = 0.92$ for $Re = 100$ and $KC = 5$. The experimental results of Dütch *et al.* [54] (symbols) are used for comparison.

motion-averaged drag and added-mass coefficients, C_d and C_i, can be evaluated by a least-square fitting method. The computed values are compared with data from the literature in Table 1 and very good agreement is observed.

3.3. Drug-thrust transition of a pitching foil

The vortex street of a pitching foil is investigated in this section for a range of flapping frequency-amplitude phases. The governing parameters of the flow are the Reynolds number $Re = U_\infty D/\nu$ and the Strouhal number

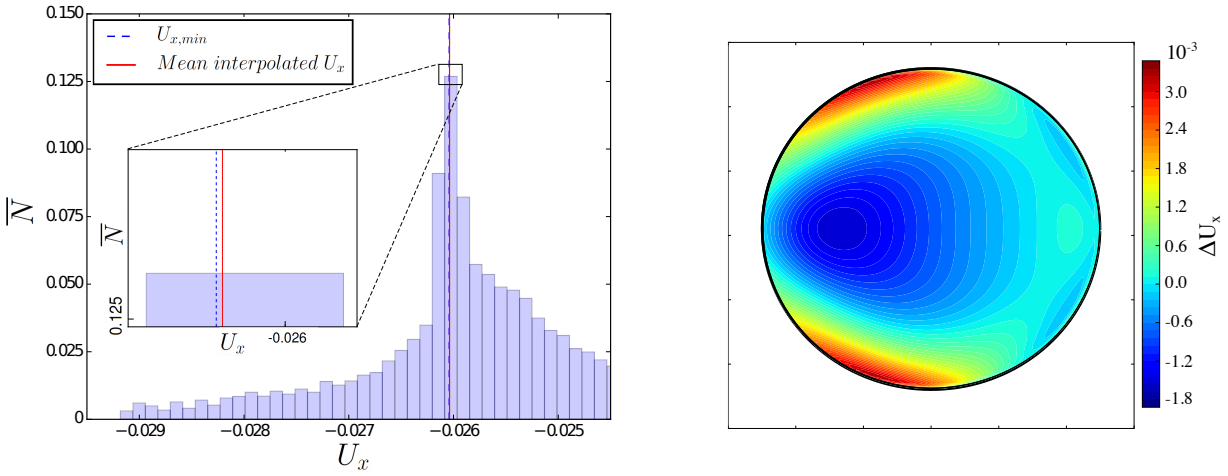

(a) (b)

Figure 6: (a) Histogram of the interpolated velocities inside the cylinder at $\phi = 0^o$ and $x = 0$, (b) Deviation of the interpolated internal velocity from the prescribed velocity at $\phi = 0^o$ and $x = 0$.

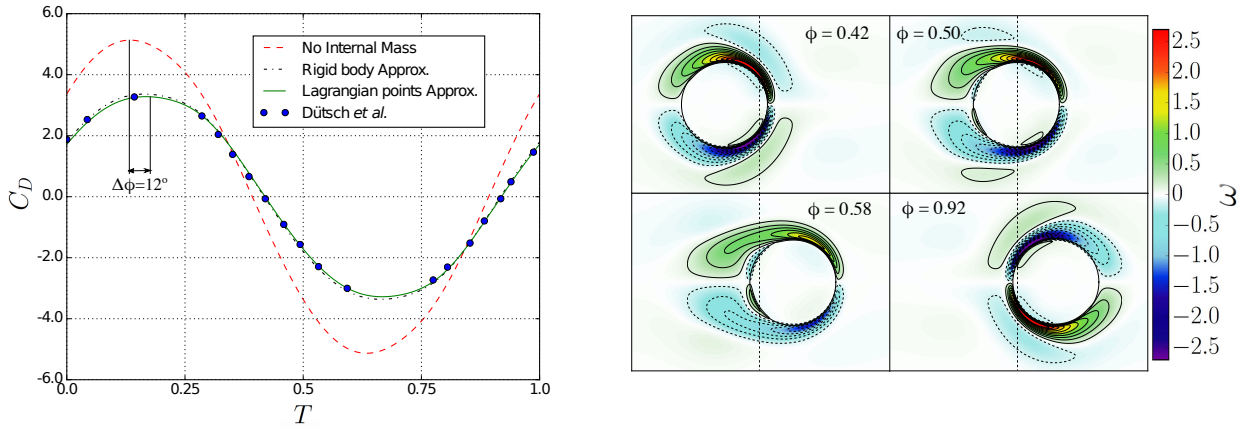

(a) (b)

Figure 7: (a) Drag coefficient over a period of a translationally oscillating circular cylinder for $Re = 100$ and $KC = 5$, (b) Instantaneous vorticity for four phase angles $\phi = 0.42$, $\phi = 0.50$, $\phi = 0.58$ and $\phi = 0.92$.

Table 1: Comparison of drag and added-mass coefficients, C_d and C_i, for a translationally oscillating circular cylinder at $Re = 100$ and $KC = 5$.

References	C_d	C_i
Dütch *et al.* [54]	2.09	1.45
Uzunoğlu *et al.* [59]	2.10	1.45
Yuan *et al.* [60]	2.10	1.45
IDF-CLBM	2.09	1.45

$Sr = fD/U_\infty$, where $U_\infty = 0.02$ is the freestream velocity, D is the foil thickness and f is the flapping frequency. The thickness to chord ratio is $D/c = 5/23$. According to Diana *et al.* [61, 62], the flapping frequency f is equivalent to the main vortex shedding frequency. The dimensionless flapping amplitude A_D is defined as $A_D = A/D$, where A is the peak-to-peak amplitude, as shown in Fig. 8. In the present study, we examine the vortex shedding at $Re_c = 1173$, where $Re_c = U_\infty c/\nu$ is the chord-based Reynolds number and $c = 300lu$ is the chord of the foil. The Strouhal number is set at $S_r = 0.22$ and four dimensionless flapping amplitudes $A_D = 0.36, 0.71, 1.07, 1.77$ are investigated.

Figures 9 and 10 show instantaneous vorticity fields and average horizontal velocity fields respectively around

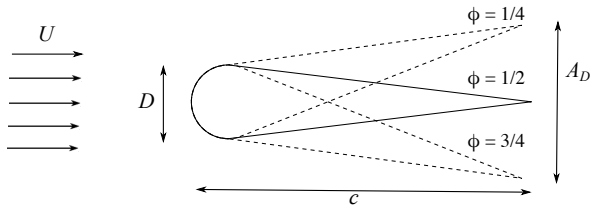

Figure 8: Schematic view of the foil and the pitching motion.

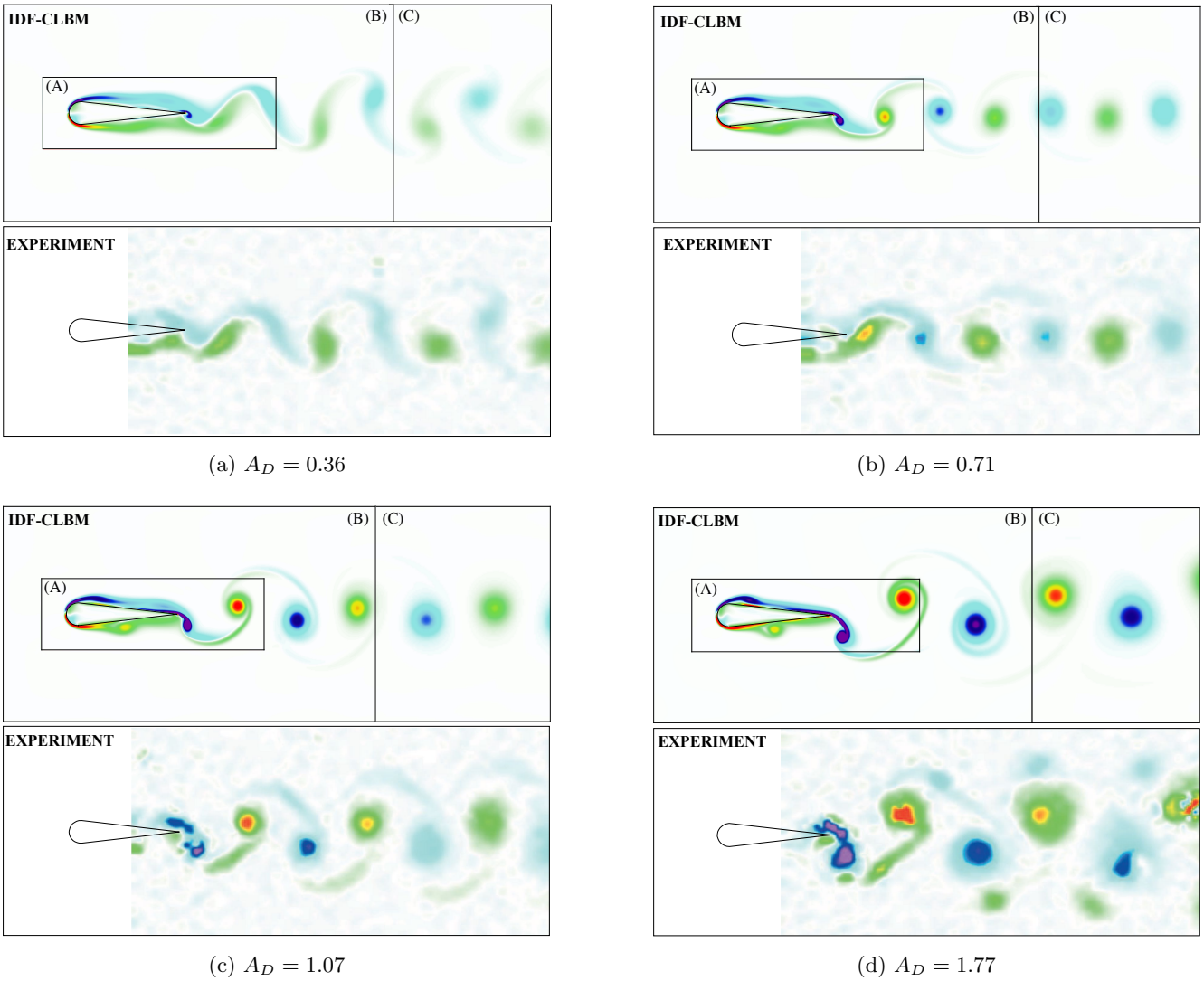

(a) $A_D = 0.36$

(b) $A_D = 0.71$

(c) $A_D = 1.07$

(d) $A_D = 1.77$

Figure 9: Instantaneous vorticity around the pitching airfoil at 0^o angle of attack, $Re = 1173$ and $Sr = 0.22$. (A), (B) and (C) denote the domains with different grid qualities with (A) being the finest domain around the foil.

the foil, for all dimensionless flapping amplitudes. The results are compared with the experimental results of Diana *et al.* [61] and good agreement is observed. The structure of the wake in Fig. 9a for a low-amplitude flapping motion, $A_D = 0.36$, resembles the features of a natural Bénard - von Kármán (BvK) vortex street. The velocity deficit behind the foil, as shown in Fig. 10a, is a result of the downstream vortices, originating from the vorticity on the sides of the foil, that tend to stay on the symmetry line of the wake. Reversal of the vortex position is observed as the dimensionless flapping amplitude increases. For $A_D = 0.71$ the downstream vortices are almost

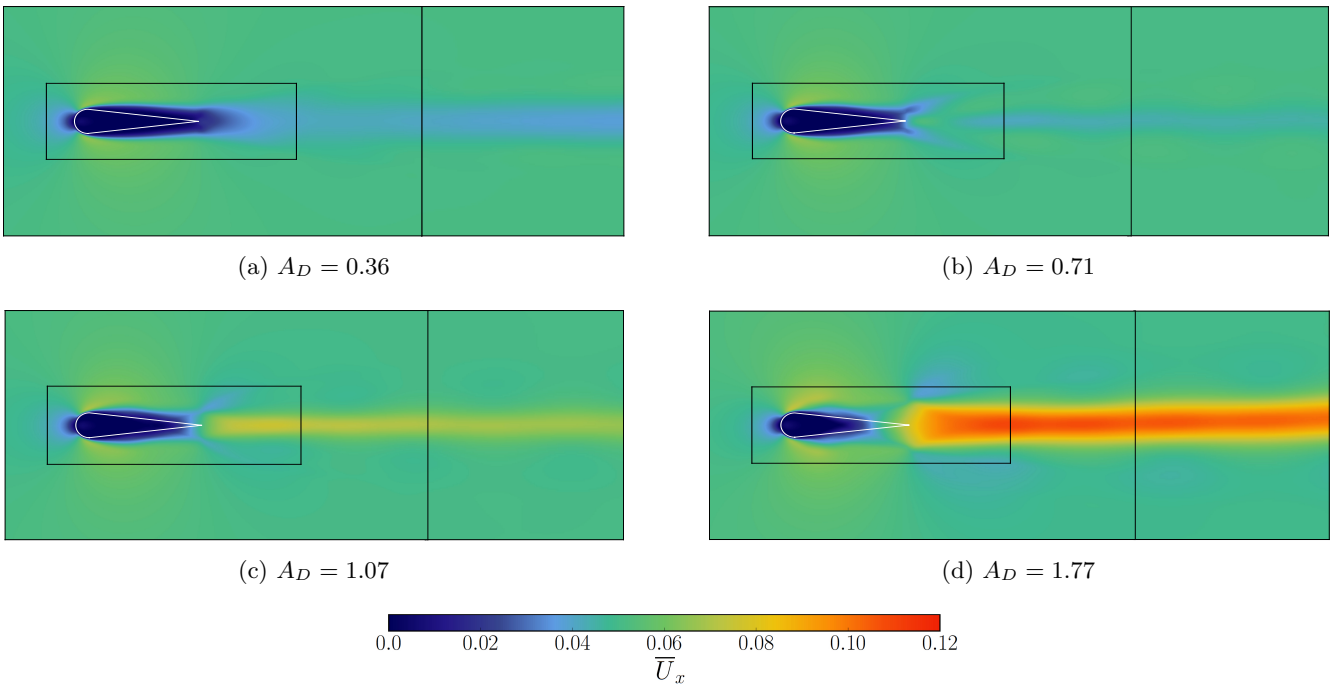

(a) $A_D = 0.36$ (b) $A_D = 0.71$

(c) $A_D = 1.07$ (d) $A_D = 1.77$

Figure 10: Time averaged horizontal velocity around the pitching airfoil at 0^o angle of attack, $Re = 1173$ and $Sr = 0.22$.

aligned, Fig. 9b, decreasing the velocity deficit of the wake significantly, Fig. 10b. Further increasing the amplitude $A_D = 1.07, 1.77$ leads to a reverse BvK vortex street, as shown in Figures 9c and 9d. Vortices created on each side of the foil are organised on the opposite sites of the symmetry line leading to an accelerating flow behind the foil, as shown in Figures 10c and 10d.

Fig. 11a shows the normalised average velocity profile at $X = 12D$ downstream from the trailing edge. Overall, the computed structures of the vortices, as well as the mean velocity fields are in very good agreement with the experimental results of Diana *et al.* [61]. It has been found that at $A_D = 1.77$ the wake is not symmetric leading to net lift force generation, as shown in Fig. 12a. For more information on the symmetry breaking of the reverse BvK vortex street the reader should refer to Diana *et al.* [62]. In Fig. 11b, we compare the computed mean

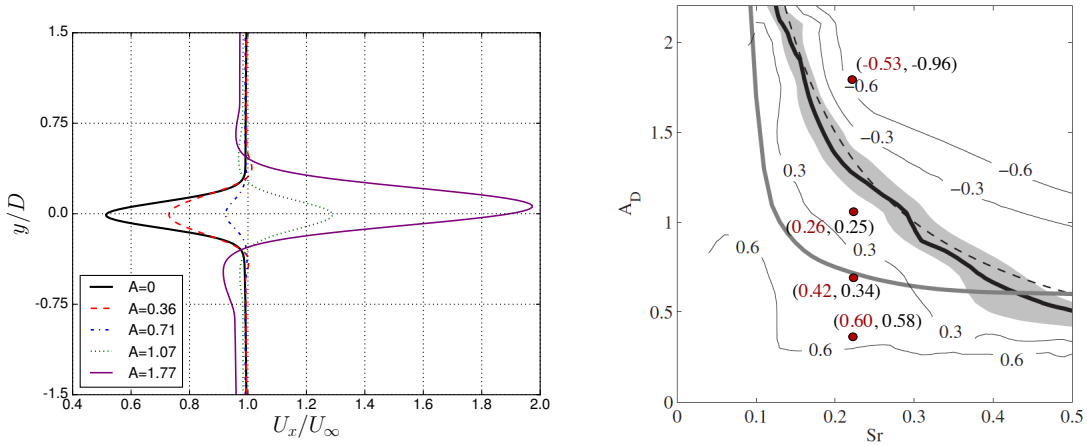

(a) (b)

Figure 11: (a) Normalised average velocity profile at $x = 12D$ downstream from the trailing edge for $A_D = 0, 0.36, 0.71, 1.07, 1.77$, (b) Contours of mean drag coefficient C_D/C_{D0} surface estimated using a momentum balance approach taken from Godoy-Diana *et al.* [61]. The present numerical results of the LPA scheme (red) and the momentum balance approach (black) are included.

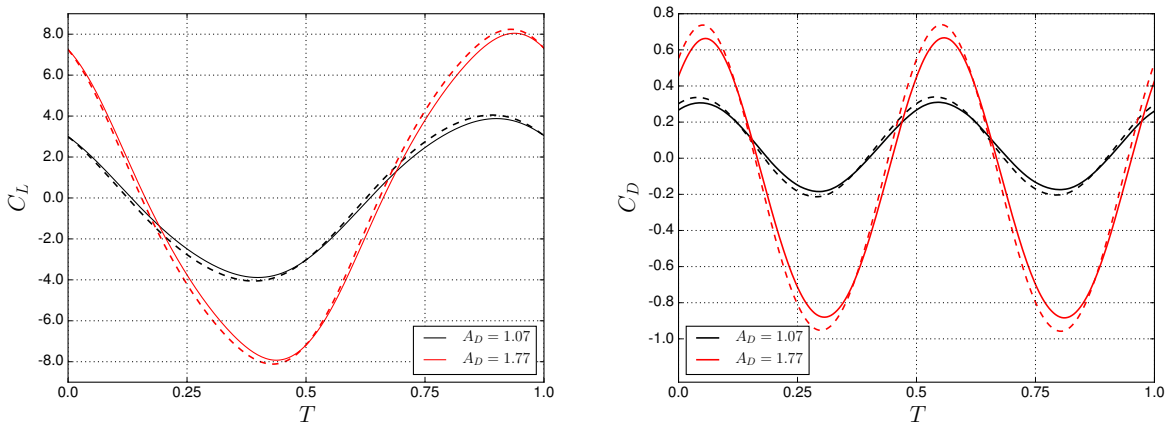

(a) (b)

Figure 12: (a) Lift and (b) drag coefficient over a flapping period for $A_D = 1.07, 1.77$. The solid and dashed lines refer to the computed coefficients with and without the LPA method.

drag coefficients with the values obtained by Diana *et al.* [61] using the momentum balance approach in a control volume around the foil. The values obtained with the LPA scheme and with the momentum balance approach are highlighted in red and black respectively. Eq. 14 is used for the computation of the mean drag coefficient with the LPA which is then normalised by its value for a rigid foil at zero angle of attack, (C_{D0}). Both methods agree well with the experimental values. However, at $A_D = 1.77$ the drag coefficient value obtained with the momentum balance approach diverges significantly from the experimental value.

The drag forces for the momentum balance approach are obtained by

$$F_D = \rho U_\infty \int [U_\infty - u(y)]dy, \tag{27}$$

where $u(y)$ is the velocity profile at $X = 12D$ downstream from the trailing edge as shown in Fig. 11a. Good agreement is observed for $A_D = 0.36, 0.71, 1.07$ where the vortex structure is fully 2-Dimensional. Finally, Fig. 12 compares the computed values for the lift and drag coefficients with and without the LPA scheme. Significant differences can be observed both in the magnitude as well as the phase of the oscillating drag coefficient.

3.4. Plunging SD7003 airfoil

The unsteady separated flow encountered by the plunging motion of a SD7003 airfoil under moderate-Reynolds-number conditions ($Re_c = 40000$) is investigated. The airfoil is set at a small static angle of attack $\alpha_0 = 4^o$ in the center of a $100c \times 100c$ computational domain, where $c = 600lu$ is the chord of the foil. The flow over a plunging SD7003 at high-frequency, low-amplitude motions has been recently investigated both numerically and experimentally [63, 64, 65, 66, 67]. The plunging motion is characterised with a reduced frequency $k = \pi fc/U_\infty = 3.93$ and a non-dimensional amplitude $h_0 = \hat{h_0}/c = 0.05$ leading to a maximum excursion of 21.5^o in the induced angle of attack.

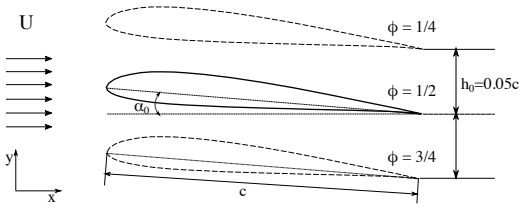

Figure 13: Schematic view of the motion of the SD7003 airfoil at a static angle of attack $\alpha_0 = 4^o$.

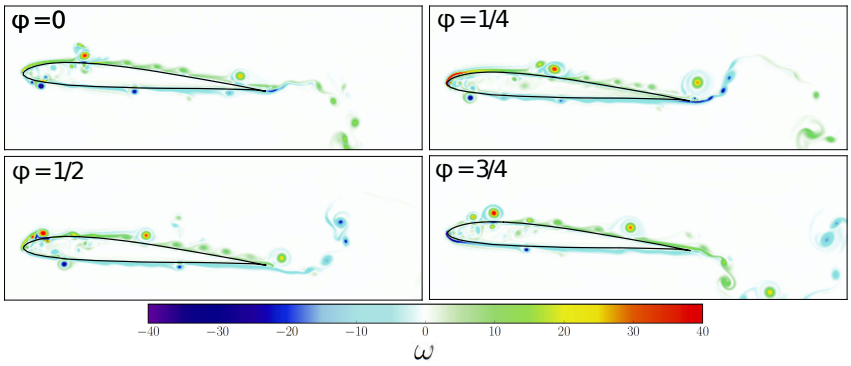

Figure 14: Vorticity field around a plunging SD7003 airfoil at $Re_c = 40000$ and four phases $\phi = 0, 1/4, 1/2, 3/4$.

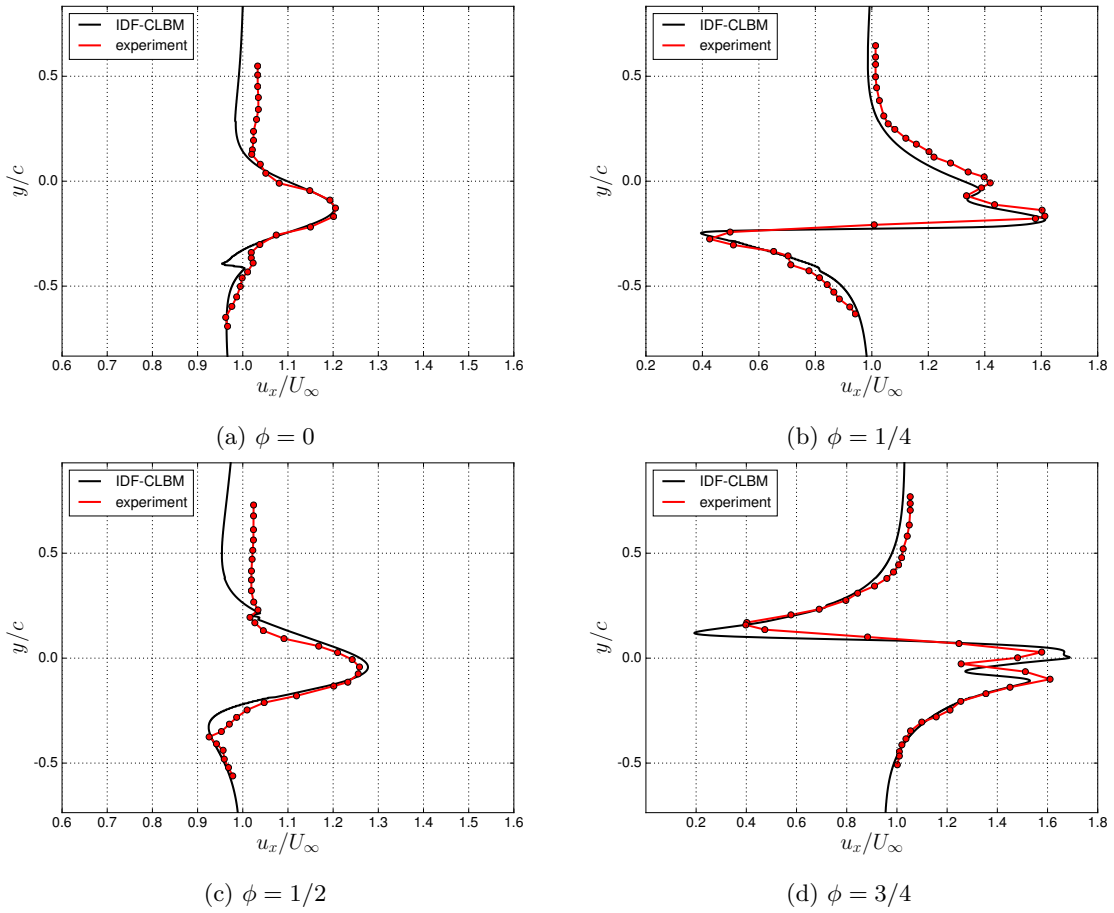

(a) $\phi = 0$ (b) $\phi = 1/4$

(c) $\phi = 1/2$ (d) $\phi = 3/4$

Figure 15: Velocity profiles for four phase angles (a) $\phi = 0$, (b) $\phi = 1/4$, (c) $\phi = 1/2$ and (d) $\phi = 3/4$ for $Re = 40000$ and $k = 3.93$. The experimental results of McGowan *et al.* [67] are used for comparison.

A detailed schematic of the motion is presented in Fig. 13. This large induced angle of attack leads to unsteady flow fields characterised by leading-edge dynamic stall vortices [63], as shown in Fig. 14.

The motion of the foil is given by

$$y(t) = \hat{h_0} \sin\left[2kF(t)t\right], \tag{28}$$

where $F(t) = 1 - e^{at}$ is a ramping function, smoothly transitioning the stationary foil to the plunging motion. The parameter a is set to $a = 9.2$.

Good agreement between the computed and the experimental phase averaged velocity fields in the near wake

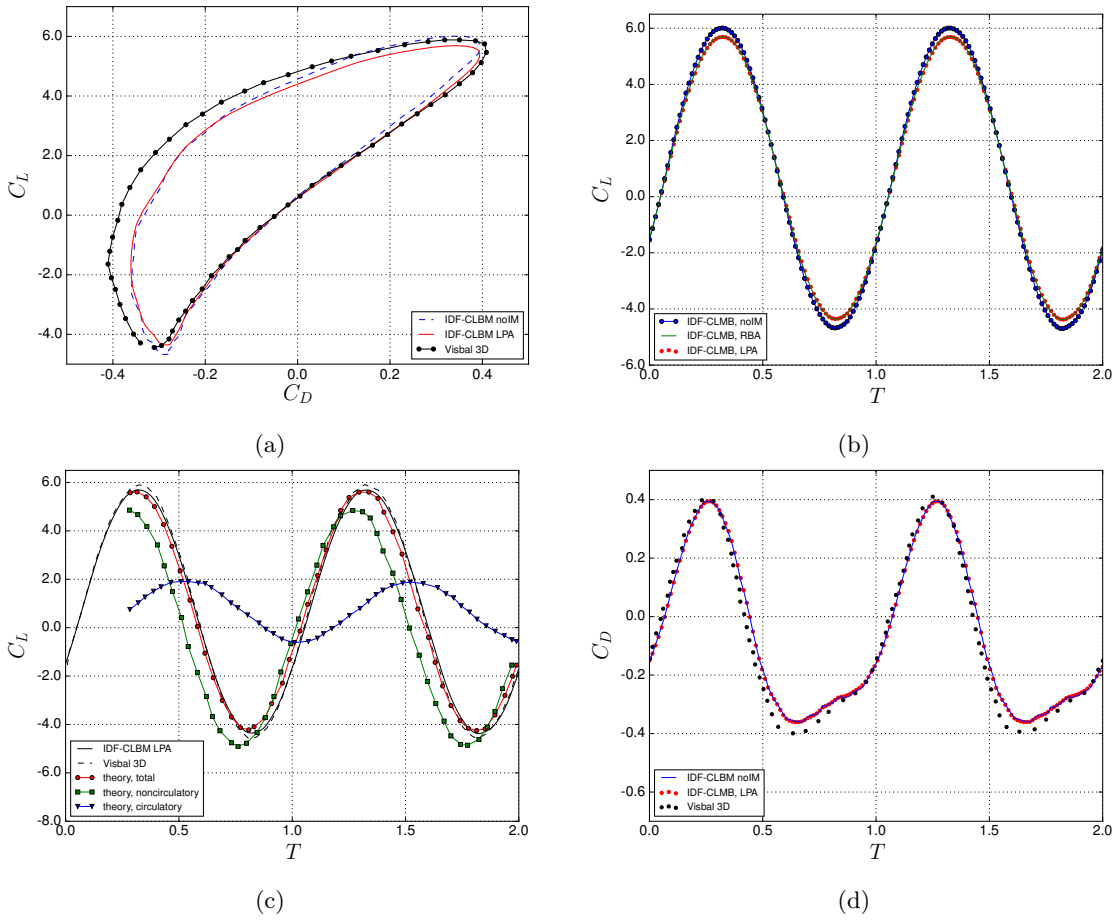

Figure 16: Computed lift and drag coefficients at $Re = 40000$,$k = 3.93$ and $\alpha_0 = 4^o$. The computational results of Visbal [63] and the theoretical inviscid results [68] are used for comparison.

$(x/c = 1.5)$ of McGowan *et al.* [67] is observed in Fig. 15. The phase averaged velocity field is computed over 20 cycles. As shown in Fig. 14, $\phi = 3/4$, the vortex shed from the upper surface boundary layer is below the trailing edge vortex shed from the lower surface. A similar observation was made by Visbal [63]. This behaviour is consistent with the jet-like mean velocity profile observed at $\phi = 0, 1/2$, shown in Fig. 15a and Fig. 15c, where the airfoil experiences the maximum vertical displacements.

Fig. 16 shows the time history of the lift and drag coefficients. The results are compared with the 3-D computational results of Visbal [63]. This specific high-frequency low-amplitude motion of the SD7003 airfoil is expected to suppress the effect of the internal mass, computed with Eq. (18), in the computation of the aerodynamic coefficients. However, an overall 5.8% decrease, computed as shown in Appendix D, and a phase difference of 1.6^o in the computed lift coefficient using the Lagrange point approximation is observed in Fig. 16b. The computed lift is found to be in good agreement both with the 3-D results of Visbal [63] and the prediction given by the inviscid theory [68]. Finally, the $C_L - C_D$ plot (Fig. 16a) over three consecutive cycle in the time-asymptotic state confirms the periodic nature of the aerodynamic forces.

3.5. Plunging and flapping NACA-0014 airfoil

The effect of the chord-wise morphing on the aerodynamic coefficients of a NACA-0014 airfoil at Reynolds number $Re = 10^4$ for a range of prescribed plunging and flapping amplitudes is investigated in this section. For moderate Reynolds number flows, Tuncer and Kaya [69] argue that flapping-wing propulsion systems are in principle more efficient than their respective rotational propeller configurations. The authors suggest that the aerodynamic loads of a flapping airfoil are strongly dominated by the leading-edge vortex dynamics and the trailing-edge vortex shedding. Murray and Howle [70] found that the aerodynamic efficiency of a flexible flapping thin foil may be significantly improved over its rigid counterpart. More recently, Miao and Ho [71] investigated the effect of flexure on

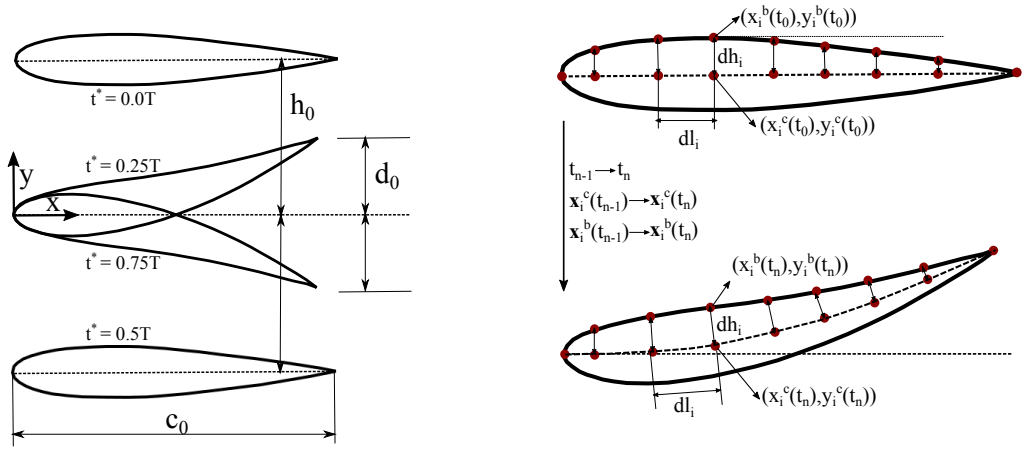

Figure 17: (a) Schematic view of the deformable NACA-0014 airfoil and the flapping motion, (b) Updated surface coordinates under prescribed deforming motion of the NACA-0014 airfoil.

the aerodynamic propulsive efficiency of a flapping flexible NACA-0014 airfoil and found that the overall propulsive efficiency is only improved for a very specific amplitude-deformation configuration. An interesting remark is the conclusion regarding the strong correlation between propulsive efficiency and reduced frequency of the oscillating motion. In this section, the flow parameters of Miao and Ho [71] are used. The airfoil undergoes a plunge motion with different flexure amplitude deformations as shown in Fig. 17a. The complex motion of the airfoil is expressed by

$$y_i(t) = -h_0\big(\cos(2\pi f(t-t_0)) + \cos(\pi)\big) - d_0\Big(\frac{x_i - x_0}{c_0}\Big)^2 \sin(2\pi f(t-t_0)), \tag{29}$$

where h_0 and a_0 denote the dimensionless amplitude of the oscillation and flexure amplitude respectively, f is the flapping frequency, x_0 is the x-coordinate of the leading edge and $c_0 = 300\delta x$ is the chord of the rigid airfoil. A reduced frequency of $k = \omega c_0/U_\infty = 2$ is used in all cases, where $U_\infty = 0.02$. The first term in the right hand side of Eq. (29) denotes the plunge motion, $h(t)$, whereas the second term describes the deforming motion, $d(t)$, which is in $\psi = 90^o$ phase difference with the plunge motion in order to optimise the propulsive efficiency based on the observations of Miao and Ho [71] and Read *et al.* [72]. What differs from the work of Miao and Ho [71] is the deformation of each point of the surface in the x-direction, $x_i^b(t_n)$. In particular, assuming a constant chord length under any flexible deformation, a three-step process is used to calculate the surface deformation of the NACA-0014 airfoil, as shown in Fig. 17b. Under symmetry conditions and assuming incompressibility of the foil under any deformation, all points on the upper surface of the foil are projected onto the chord line. The discretisation lengths $dh_i(t_0)$ and $dl_i(t_0)$ are kept constant under any deformation.

1. Apply Eq. (29) to the chord line and compute $y_i^c(t_n)$. Under the constraint $dl_i(t_n) = dl_i(t_0)$ compute $x_i^c(t_n)$ using the following equation

$$x_i^c(t_n) = x_{i-1}^c(t_n) + \sqrt{dl_i(t_0)^2 - (y_i^c(t_n) - y_{i-1}^c(t_n))^2}, \tag{30}$$

   where the superscript c refers to the chord of the foil.
2. Compute the chord tangents from Eq. 29, $(dy_i(t)/dx)$, and the compute the wall normals for all points i using

$$n_i^c(t_n) = [A_0(\sin(2\pi ft)/c^2)(x_i^c(t_n) - x_0^c(t_n))]^{-1} \tag{31}$$

3. Under the incompressibility constraint $dh_i(t_n) = dh_i(t_0)$, compute the foil surface deformation $x_i^b(t_n), y_i^b(t_n)$ using

$$y_i^b(t_n) = n_i^c(t_n)\sqrt{dh_i(t_0)^2/(1 + n_i^c(t_n)^2)} + y_i^c(t_n), \tag{32}$$

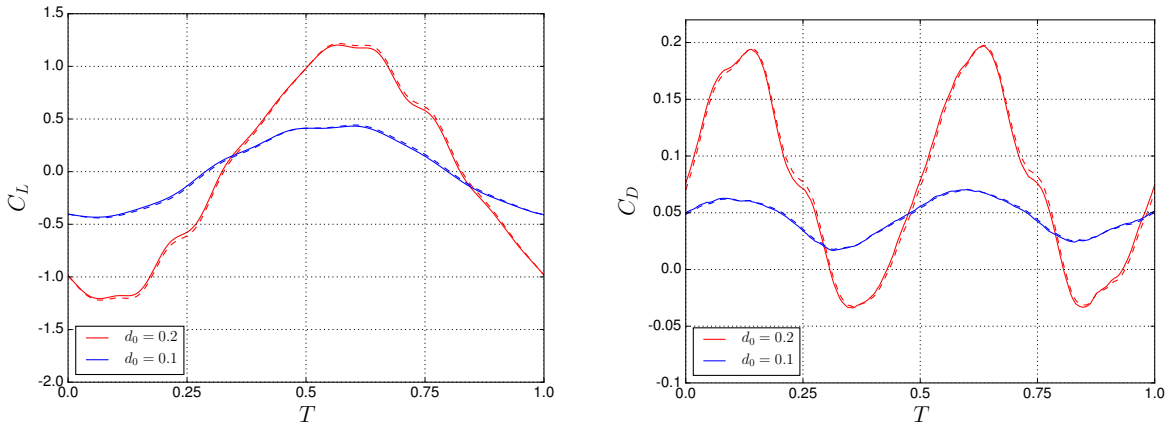

(a) (b)

Figure 18: Lift and Drag coefficients for rigid and flexible foil at plunging amplitude $h_0 = 0.0c_0$. The solid and dashed lines refer to the results with and without the LPA respectively.

$$x_i^b(t_n) = (y_i^b(t_n) - y_i^c(t_n))/(n_i^c(t_n)) + x_i^c(t_n), \tag{33}$$

where the superscript b refers to the surface of the foil.

3.5.1. Case 1 and 2: Deforming amplitudes $d_0 = 0.1c_0$ and $d_0 = 0.2c_0$

A chord-wise deforming motion with $d_0 = 0.1c_0$ and $d_0 = 0.2c_0$ is prescribed where no flapping motion is imposed to the foil. Fig. 18 shows the time evolution of the lift and drag coefficients under one period of oscillation. Since the overall motion of the foil is small, the effect of the internal mass in the computation of the aerodynamic coefficients is not dominant. As shown in Fig. 18a much higher values of the lift coefficient are observed for $d_0 = 0.2c_0$. The stronger pressure gradient acting on the foil at a deformation amplitude $d_0 = 0.2c_0$, is showed in Fig. 19.

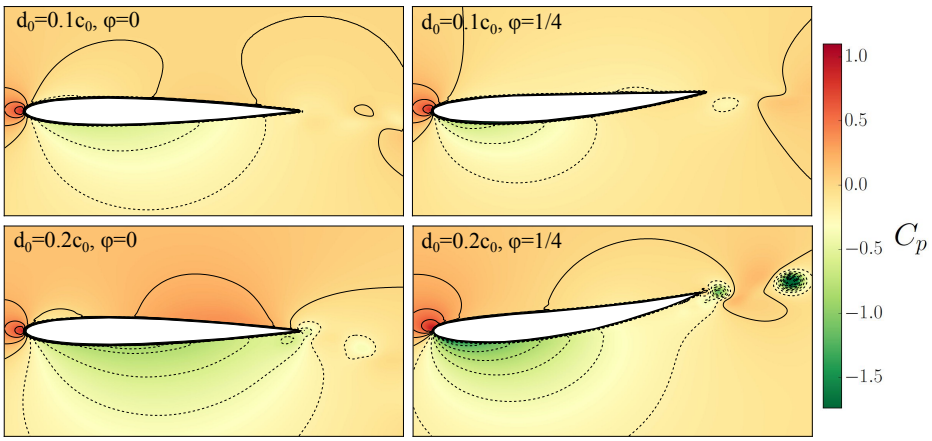

Figure 19: Pressure coefficient contour around a deformable NACA-0014 airfoil at $Re = 10000$, $d_0 = 0.1c_0, 0.2c_0$ and phase angles $\phi = 0, 1/4$.

The computed time-averaged drag coefficient is $\overline{C}_D = 0.0557$ for the rigid NACA-0014 airfoil and $\overline{C}_D = 0.0457$ and $\overline{C}_D = 0.0763$ for the deformation amplitudes $d_0 = 0.1c_0$ and $d_0 = 0.2c_0$ respectively. The amplitude of the oscillation in the drag coefficient is much higher for $d_0 = 0.2c_0$. As shown in Fig. 20, between phases $\phi = 0$ and $\phi = 0.25$ the vorticity profiles around the airfoil differ significantly. For the larger deformation amplitude case, the vorticity generated at the trailing edge rolls over into smaller vortices that are shed downstream. Overall, under small deforming amplitudes, no significant improvement in the time-averaged thrust generation is observed.

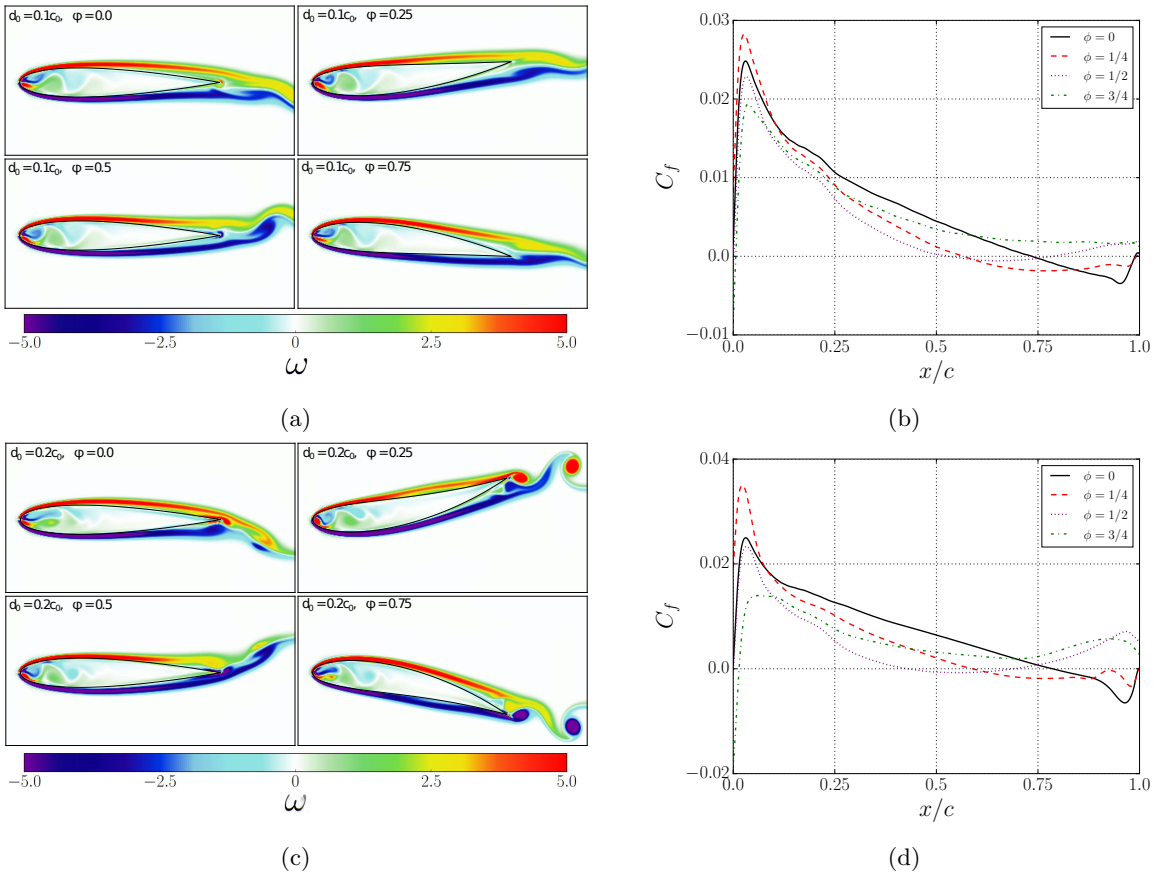

Figure 20: Vorticity field around a deformable NACA-0014 airfoil at $Re = 10000$ for (a) $d_0 = 0.1c_0$ and (c) $d_0 = 0.2c_0$. Skin friction coefficient on lower airfoil surface at phases $\phi = 0, 1/4, 1/2, 3/4$ for deforming amplitudes (b) $d_0 = 0.1c_0$ and (d) $d_0 = 0.1c_0$.

3.5.2. Cases 3, 4 and 5: Plunging amplitude $h_0 = 0.2c_0$ and deforming amplitudes $d_0 = 0.1c_0, 0.2c_0$

The flow around a flapping and deforming NACA-0014 airfoil at $Re = 10000$ is investigated in this section. The prescribed flapping amplitude is $h_0 = 0.2c_0$.

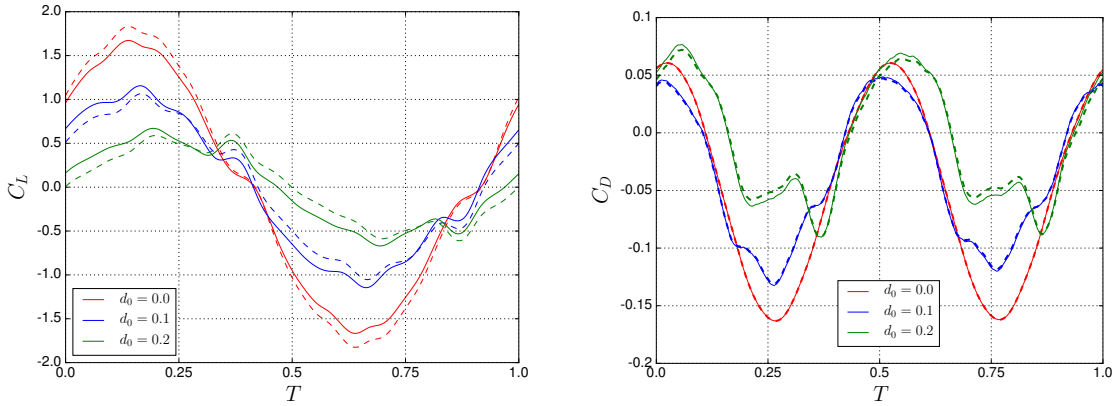

Figure 21: Lift and Drag coefficients for rigid and deformable NACA-0014 airfoil at plunging amplitude $h_0 = 0.2c_0$ and deforming amplitudes $\alpha_0 = 0.0c_0, 0.1c_0, 0.2c_0$. The solid and dashed lines refer to the results with and without the LPA respectively.

We examine the cases of a rigid flapping foil and a deforming flapping foil with flexure amplitudes $d_0 = 0.1c_0$ and $d_0 = 0.2c_0$. Fig. 21 shows the time evolution of the lift and drag coefficients under one period of oscillation. The effect of the internal mass in the computation of the aerodynamic coefficients is significant, especially in the direction of the flapping motion. For $d_0 = 0.0c_0$ the internal mass corrections are stronger around the regions of the extremes, Fig. 21a. However, under the deforming motions, the corrections in the lift coefficient are important throughout the entire period of oscillation. It is shown that the present scheme can very accurately capture the momentum of the internal fluid even in very complex motions. It is observed that as the flexure amplitude d_0 increases the extremes in the lift coefficient decrease. In the higher deforming amplitude case, $d_0 = 0.2c$, the overall periodic profile of both the lift and drag coefficients significantly differs from that of the rigid flapping foil. As shown in Fig. 21a, two peaks of approximately the same magnitude are observed between $t^* = 0$ and $0.5T$ and $t^* = 0.5T$ and $1.0T$. Similar observations can be made for the drag coefficient, Fig. 21b. The aerodynamic loads at this specific medium-amplitude low-frequency configuration are shown to be strongly dominated by the leading-edge vortex dynamics and the trailing-edge vortex shedding. Fig. 22 shows the skin friction coefficient and vorticity snapshots around the foil at phases $\phi = 0, 1/4, 1/2, 3/4$ and deforming amplitudes $d_0 = 0.1c_0$ and $d_0 = 0.2_0$.

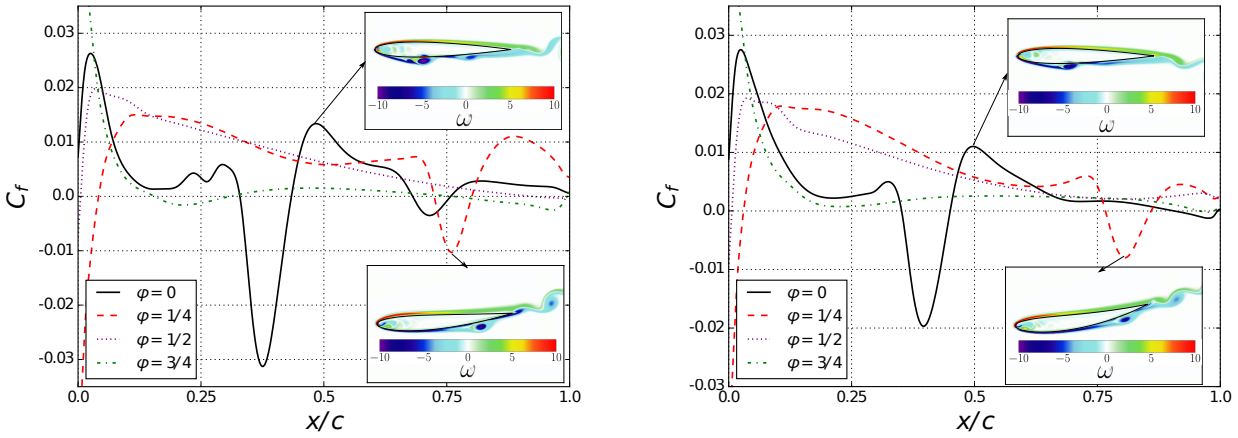

Figure 22: Skin friction coefficient on lower airfoil surface at phases $\phi = 0, 1/4, 1/2, 3/4$ for plunging amplitude $h_0 = 0.2c_0$ and deforming amplitudes (a) $d_0 = 0.1c_0$ and (b) $d_0 = 0.2c_0$.

In both cases, the position of the leading-edge vortex at $\phi = 0$ is approximately the same. However, for $d_0 = 0.1c_0$ a smaller amplitude vortex is located at 72% of the chord length leading to a trailing-edge vortex at $\phi = 0.25$. For the rigid plunging NACA-0014 aifoil, the period-average computed drag coefficient is $\overline{C}_D = -0.053$. The period-averaged drag force for the investigated deformation amplitudes $d_0 = 0.1c_0$ and $d_0 = 0.2c_0$ is $\overline{C}_D = -0.036$ and $\overline{C}_D = -0.007$ respectively. The period-averaged thrust force decreases from that of a rigid foil.

3.5.3. Case 6, 7 and 8: Plunging amplitude $h_0 = 0.4c_0$ and deforming amplitudes $d_0 = 0.1c_0, 0.3c_0$

The last cases in this section investigate the flow around a moving NACA-0014 airfoil at $Re = 10000$ with plunging amplitude $h_0 = 0.4c_0$ and deforming amplitudes $d_0 = 0.0c_0$, $d_0 = 0.1c_0$ and $d_0 = 0.3c_0$. The time evolution of the lift and drag coefficients under one period of oscillation for the three investigated cases are shown in Fig. 23. In this high-amplitude low-frequency motion configurations the internal mass effects are quite significant in the computation of the aerodynamic coefficients. The present LPA scheme can accurately capture the internal mass effects. Overall, as shown in Fig. 23a, the magnitude of the lift coefficient decreases drastically as the flexure amplitude d_0 increases. The difference in the lift force generation can be partially explained by investigating the pressure gradient acting on the foil at different phases of the oscillation.

As shown in Fig. 24, the leading-edge vortex formation and the subsequent trailing-edge vortex shedding dynamically affect the pressure around the foil. For the high deformation amplitude case, a significant observable difference in the trend of the lift coefficient over the period is observed. Similar observations can be made for the periodic behaviour of the drag coefficient, Fig. 23b. Overall, an improvement in the period-averaged thrust generation is observed for $d_0 = 0.1c_0$ where $\overline{C}_D = -0.249$ with respect to the rigid flapping foil case where $\overline{C}_D = -0.242$. The aerodynamic loads of the NACA-0014 airfoil at this specific high-amplitude low-frequency

configuration are shown to be strongly dominated by the leading-edge vortex dynamics and the trailing-edge vortex shedding.

Fig. 25 shows the skin friction coefficient and vorticity snapshots around the foil at phases $\phi = 0, 1/4, 1/2, 3/4$ and deforming amplitudes $d_0 = 0.1c_0$ and $d_0 = 0.3c_0$. In both cases, the position of the two leading-edge vortices at $\phi = 0$ is approximately the same. However, the structure of the vortices differs significantly leading to subsequently different vortex shedding dynamics. As shown in Fig. 25b, at $\phi = 3/4$ and $d_0 = 0.3c_0$ the structure of the trailing-edge vortices is more coherent and both vortices are closer to the surface of the foil.

It has been shown that the Lagrangian point approximation method can accurately capture the effects of the internal mass under various plunging-deforming configurations including both linear and angular motions. The effect of the deformation amplitude on the computation of the aerodynamic forces has been investigated and shown that the leading-edge vortex formation and the subsequent trailing-edge vortex shedding dominantly affect both the magnitude and the trend of the aerodynamic loads in all investigated plunging amplitudes $h_0 = 0.0c_0 - 0.4c_0$ and flexure amplitudes $d_0 = 0.0c_0 - 0.3c_0$. For zero plunging amplitude motions, an increase in both the lift and drag forces has been found. However, in the combined plunging-deforming motions, different aerodynamic behaviours have been observed. The formation of the leading-edge vortex seems to be mainly affected by the plunging amplitude, whereas the vortex transition along the surface of the foil and the respective thrust-indicative wake structure are strongly influenced by the deforming amplitude. However, in order to generalise the deformation effects, additional configurations must be examined. That includes the effect of the phase angle between the plunging and deforming motion, the effect of the reduced frequency and the effect of the Reynolds number.

3.6. Numerical accuracy of the Lagrange point approximation method

In this section the computational efficiency and accuracy of the Lagrangian point approximation method is investigated in order to define an optimum number of internal points and accurately represent the effects of the internal mass in the computation of the aerodynamic coefficients. First, consider an immersed body with a surface area A_Ω and define a number of internal Lagrangian points N_{int} with volume ΔV_{int}. As described in Section 2.3.2, the scaling factor is defined as $S_c = A_\Omega / N_{int}$. In this section, the accuracy of the LPA will be investigated for $S_c = 1.0$, $S_c = 2.0$ and $S_c = 4.0$. In all cases the internal Lagrangian points are equally spaced inside A_Ω. In order to quantify the effect of the LPA for the different scaling factors we use a modified normalised percentage error calculation procedure, shown in Appendix D. The normalised percentage errors of the lift and drag coefficients for all the cases investigated in this study are presented in Table 2. All errors are computed with respect to the aerodynamic coefficients as computed without considering the effects of the internal mass.

From Table 2 it is clear that the accuracy of the LPA is not significantly affected when 25%, ($S_c = 4$), of the initial internal Lagrangian points is used. It should be noted however, that the initial number of Lagrangian points N_{int}, ($S_c = 1$), should be big enough in order to accurately capture the internal mass effects. There are effects

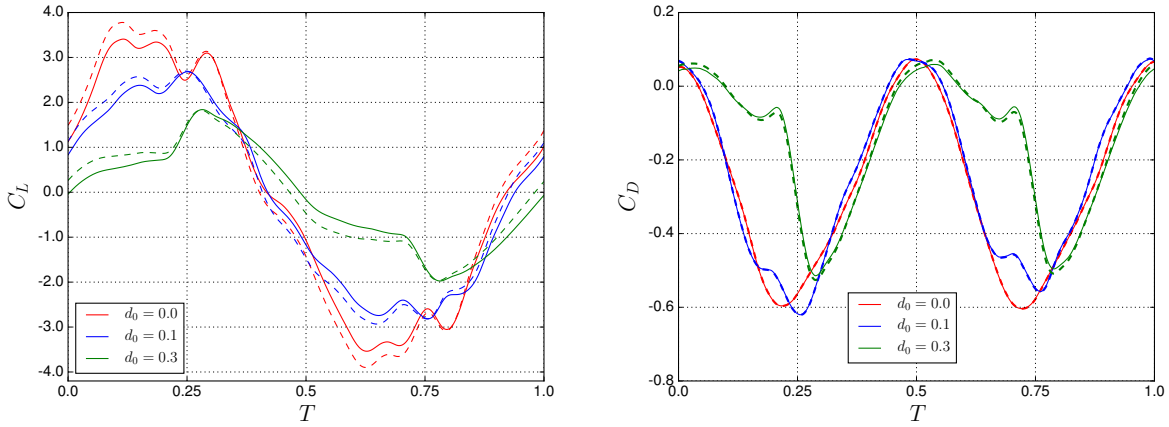

(a) (b)

Figure 23: Lift and Drag coefficients for rigid and deformable NACA-0014 airfoil at plunging amplitude $h_0 = 0.4c_0$ and deforming amplitudes $\alpha_0 = 0.0c_0, 0.1c_0, 0.3c_0$. The solid and dashed lines refer to the results with and without the LPA respectively.

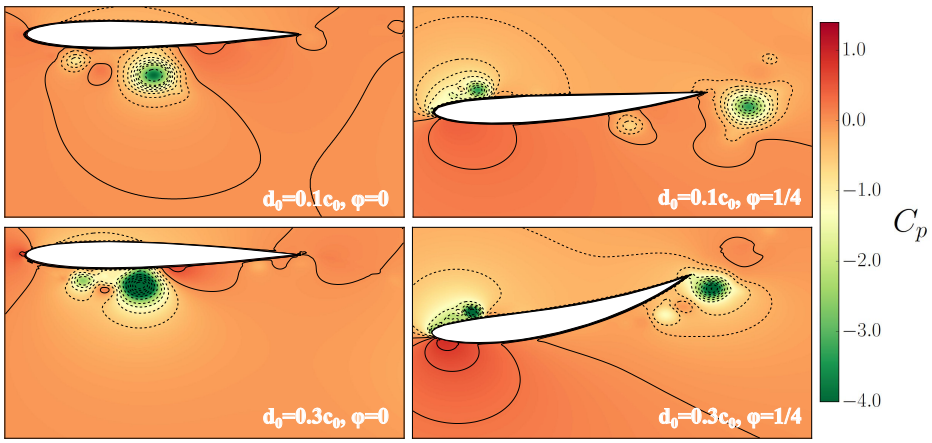

Figure 24: Pressure coefficient contour around a plunging deformable NACA-0014 airfoil at $Re = 10000$, $h = 0.4c_0$, $d_0 = 0.1c_0, 0.3c_0$ and phase angles $\phi = 0, 1/4$.

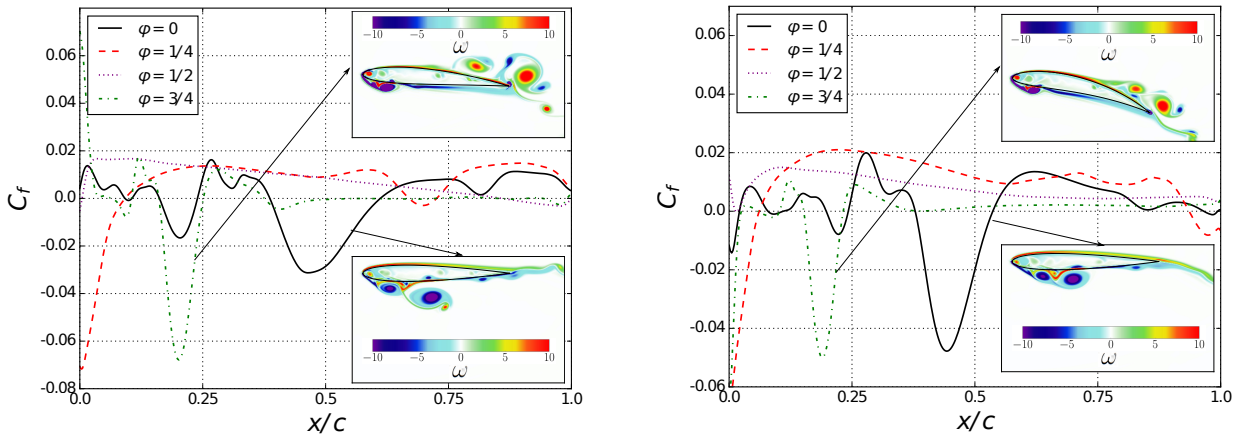

(a) (b)

Figure 25: Skin friction coefficient on lower airfoil surface at phases $\phi = 0, 1/4, 1/2, 3/4$ for plunging amplitude $h_0 = 0.4c_0$ and deforming amplitudes (a) $d_0 = 0.1c_0$ and (b) $d_0 = 0.3c_0$.

however, that cannot be directly extracted from the normalised percentage differences. As shown in Fig. 26b, the internal forces differ both in magnitude and in phase when only a part of the internal Lagrangian points is used. In the present test cases where the motion of the body is prescribed those differences are negligible. However, in cases where the motion of the immersed body is affected by the fluid forces acting on it, a more careful consideration regarding the number of Lagrangian points is required. In Table 3, the maximum absolute percentage differences on the lift and drag coefficients for the flow around the NACA-0014 airfoil with $h_0 = 0.4c_0$ is shown. A similar behaviour is observed, indicating that for the cases studied in this paper it is sufficient to represent the effects of the internal mass using 25% of N_{int}.

4. Conclusions

The present coupled iterative force-correction immersed-boundary cascaded lattice-Boltzmann solver has been applied to viscous fluid flows around moving and deformable boundaries and found to be computationally accurate and robust. We have extensively investigated the effects of the internal mass in the computation of the aerodynamic loads and shown that the Lagrangian points approximation scheme significantly improves the numerical accuracy over a wide range or Reynolds numbers and frequency-amplitude motion configurations. The robustness and numerical accuracy of the present scheme is demonstrated by studies of unsteady flows around an oscillating cylinder, a pitching foil, a plunging foil and a plunging and flapping foil. The present results compare well with other experimental and numerical results found in the literature.

Table 2: Numerical accuracy of the Lagrange point approximation method for three scaling factors $S_c = 1.0$, $S_c = 2.0$ and $S_c = 4.0$. All numbers are expressed as % differences.

Case	Configuration	C_L			C_D		
		$E_N^{Sc=1}$	$E_N^{Sc=2}$	$E_N^{Sc=4}$	$E_N^{Sc=1}$	$E_N^{Sc=2}$	$E_N^{Sc=4}$
Cylinder	$A_m = 2.5D/\pi$	-	-	-	34.051	34.049	34.048
Pitching foil	$A_D = 0.36D$	7.974	7.970	7.961	1.466	1.471	1.470
	$A_D = 0.71D$	7.098	7.094	7.086	6.108	6.106	6.090
	$A_D = 1.07D$	6.250	6.247	6.239	10.278	10.272	10.257
	$A_D = 1.77D$	5.165	5.162	5.157	10.954	10.948	10.925
SD7003	$h_0 = 0.05c$	5.435	5.433	5.428	1.084	0.992	1.114
NACA-0014	$h_0 = 0.0c_0, \quad d_0 = 0.1c_0$	3.568	3.567	3.567	1.859	1.867	1.864
	$h_0 = 0.0c_0, \quad d_0 = 0.2c_0$	2.573	2.574	2.574	3.263	3.270	3.267
	$h_0 = 0.2c_0, \quad d_0 = 0.0c_0$	7.739	7.741	7.739	0.157	0.225	0.294
	$h_0 = 0.2c_0, \quad d_0 = 0.1c_0$	13.947	13.945	13.952	1.348	1.403	1.453
	$h_0 = 0.2c_0, \quad d_0 = 0.2c_0$	25.270	25.266	25.277	7.371	7.372	7.318
	$h_0 = 0.4c_0, \quad d_0 = 0.0c_0$	10.499	10.498	10.500	0.127	0.182	0.206
	$h_0 = 0.4c_0, \quad d_0 = 0.1c_0$	12.634	12.633	12.635	2.993	3.063	3.247
	$h_0 = 0.4c_0, \quad d_0 = 0.3c_0$	18.332	18.330	18.334	3.812	3.807	3.828

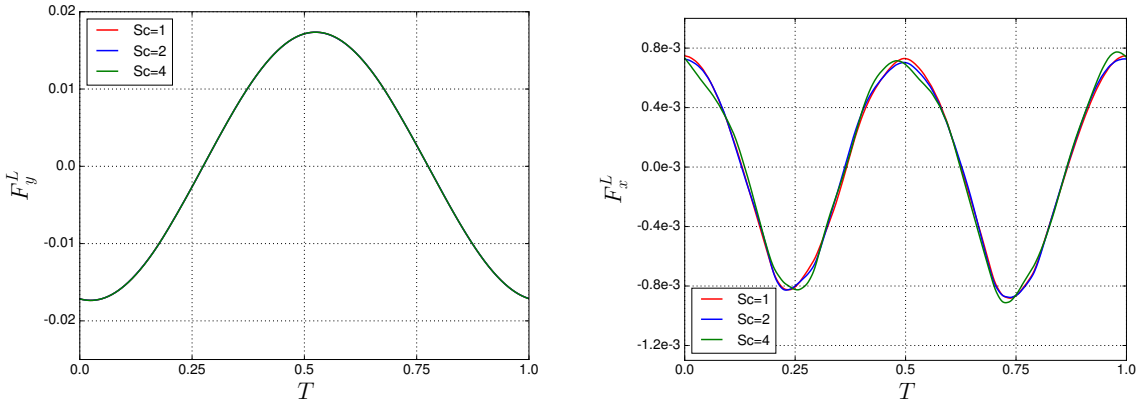

(a) (b)

Figure 26: Time history of internal Lagrangian forces (F_y^L, F_x^L) for $S_c = 1, 2, 4$ at plunging amplitude $h_0 = 0.4c_0$ and deforming amplitude $d_0 = 0.3c_0$.

Table 3: Maximum absolute percentage difference on the computed lift and drag coefficient for three scaling factors $S_c = 1.0$, $S_c = 2.0$ and $S_c = 4.0$.

Case	Configuration	C_L			C_D		
		$E_m^{Sc=1}$	$E_m^{Sc=2}$	$E_m^{Sc=4}$	$E_m^{Sc=1}$	$E_m^{Sc=2}$	$E_m^{Sc=4}$
NACA-0014	$h_0 = 0.4c_0, \quad d_0 = 0.0c_0$	11.751	11.748	11.751	0.475	0.609	0.820
	$h_0 = 0.4c_0, \quad d_0 = 0.1c_0$	15.025	15.022	15.031	1.513	1.506	1.523
	$h_0 = 0.4c_0, \quad d_0 = 0.3c_0$	28.356	28.352	28.361	6.860	6.783	7.231

The importance of the internal mass effects on the computation of the aerodynamic loads of moving boundaries, where the boundary motion is prescribed, has been demonstrated. Significant differences both in the magnitude phase of the loads have been found. Overall, a strong dependence of the internal forces on the motion characteristics (amplitude of oscillation and frequency) has been observed. In linear motions, both the rigid body (RBA) and the Lagrangian points (LPA) approximations accurately estimate the linear momentum of the immersed body. For the flow around an oscillating cylinder, at $Re = 100$, and around a plunging SD7003 foil, at $Re_c = 40000$, the aerodynamic loads have been accurately computed with both schemes. Neglecting the internal mass effects results in over-prediction of the aerodynamic loads by $10\% - 50\%$. However, as the internal velocity is strongly influenced by the force spreading operation in the IBM, an approximation of the internal momentum with a prescribed value

would lead to inaccuracies in more complex motions. The present IDF-CLBM solver has been shown to accurately capture the vortex dynamics around the plunging SD7003 foil and good agreement between the computed and the experimental time-averaged wake profiles has been observed. In angular and deformable motions, where the rigid body approximation is not valid, the momentum of the internal fluid has been successfully computed with the Lagrangian point approximation scheme. Initially, the flow around a pitching foil has been examined and compared with experiments. The computed drag coefficient LPA values have been found to be in good agreement with experimental values. The vortex structure computed with the present IDF-CLBM scheme agrees well with the experimental structure for a wide range of flapping amplitudes. Finally, the flow around a flapping deformable NACA-0014 airfoil, at $Re = 10000$, and various amplitude/deformation configurations has been investigated in order to demonstrate the robustness of our scheme. As expected, a strong dependence of the aerodynamic loads on the leading and trailing-edge vortex dynamics has been observed. Overall, the periodic profile of the aerodynamic loads is strongly related to the motion characteristics and is significantly affected by the internal mass effects.

The LPA is shown to be an accurate and flexible method of incorporating the effects of the internal mass in the computation of the aerodynamic loads around moving objects. We conclude that for flows around moving and deformable bodies, where the motion of the body is prescribed, using 25% of the total internal Lagrangian points is sufficient to capture the momentum of the internal fluid whilst maintaining the accuracy of the computation and reducing the computational overhead by 4%. For fully coupled fluid structure interaction (FSI) problems including deformable geometries further investigations and alternative treatments might be required.

Appendix A. Immersed boundary method - Basic formulation

The governing equations of the immersed boundary formulation for viscous incompressible flows are

$$\nabla \cdot \mathbf{u} = 0, \tag{A.1}$$

$$\rho(\frac{\partial \mathbf{u}}{\partial t} + \mathbf{u} \cdot \nabla \mathbf{u}) + \nabla p = \mu \triangle \mathbf{u} + \mathbf{g}, \tag{A.2}$$

$$\mathbf{g}(\mathbf{x}, t) = \int_{\mathscr{E}} \mathbf{G}(s, t)\delta(\mathbf{x} - \mathbf{X}_{\mathscr{L}}(s, t))ds, \tag{A.3}$$

$$\frac{\partial \mathbf{X}_{\mathscr{L}}(s, t)}{\partial t} = \mathbf{U}(\mathbf{X}_{\mathscr{L}}(s, t), t) = \int_{\mathscr{E}} \mathbf{u}(\mathbf{x}, t)\delta(\mathbf{x} - \mathbf{X}_{\mathscr{L}}(s, t))d\mathbf{x}, \tag{A.4}$$

$$\mathbf{G}(s, t) = \mathbf{S}(\mathbf{X}_{\mathscr{L}}(s, t), t). \tag{A.5}$$

Eqs. (A.1 - A.2) are the Eulerian Navier-Stokes equations with external forces $\mathbf{g}$ for the fluid domain $\Omega(t)$, whereas Eqs. (A.3 - A.5) are the equations in Lagrangian formalism for the immersed boundary $\mathscr{E}(t)$. $\mathbf{X}_{\mathscr{L}}$, $\mathbf{U}$, $\mathbf{G}$ are the position of the IB in Lagrangian coordinates, the IB velocity and force density, respectively. $\mathbf{x}$, $\mathbf{u}$, $\mathbf{g}$, ρ and p are the Cartesian coordinates, fluid velocity, external force density, density and pressure, respectively. δ is the delta function which can be expressed as a product of 1-Dimensional functions $\delta_h(\mathbf{x}-\mathbf{X}_{\mathscr{L}}) = h^{-d}\prod_{i=1}^{d}\phi\Big(\frac{x^i - X_{\mathscr{L}}{}^i}{h}\Big)$, where d is the dimensionality of the problem and h is the grid spacing.

Appendix B. Equilibrium distributions for the CLBM formulation

Chosing the nominal moment basis and the orthogonalised matrix $\mathbf{K}$ [42], the equlibrium distribution contains higher order velocity terms as compared to the standard LBM [6].

$$f_0^{eq} = 4/9\rho - 2/3\rho(u_x^2 + u_y^2) + \rho u_x^2 u_y^2, \tag{B.1a}$$
$$f_1^{eq} = 1/9\rho + 1/3\rho u_x + 1/2\rho u_x^2 - 1/6\rho(u_x^2 + u_y^2) - 1/2\rho(u_x u_y^2 + u_x^2 u_y^2), \tag{B.1b}$$
$$f_2^{eq} = 1/9\rho + 1/3\rho u_y + 1/2\rho u_y^2 - 1/6\rho(u_x^2 + u_y^2) - 1/2\rho(u_y u_x^2 + u_x^2 u_y^2), \tag{B.1c}$$
$$f_3^{eq} = 1/9\rho - 1/3\rho u_x + 1/2\rho u_x^2 - 1/6\rho(u_x^2 + u_y^2) + 1/2\rho(u_x u_y^2 - u_x^2 u_y^2), \tag{B.1d}$$
$$f_4^{eq} = 1/9\rho - 1/3\rho u_y + 1/2\rho u_y^2 - 1/6\rho(u_x^2 + u_y^2) + 1/2\rho(u_y u_x^2 - u_x^2 u_y^2), \tag{B.1e}$$
$$f_5^{eq} = 1/36\rho + 1/12\rho(u_x + u_y + u_x^2 + u_y^2) + 1/4\rho(u_x u_y + u_x^2 u_y + u_x u_y^2 + u_x^2 u_y^2), \tag{B.1f}$$
$$f_6^{eq} = 1/36\rho + 1/12\rho(-u_x + u_y + u_x^2 + u_y^2) + 1/4\rho(-u_x u_y + u_x^2 u_y - u_x u_y^2 + u_x^2 u_y^2), \tag{B.1g}$$
$$f_7^{eq} = 1/36\rho + 1/12\rho(-u_x - u_y + u_x^2 + u_y^2) + 1/4\rho(u_x u_y - u_x^2 u_y - u_x u_y^2 + u_x^2 u_y^2), \tag{B.1h}$$
$$f_8^{eq} = 1/36\rho + 1/12\rho(u_x - u_y + u_x^2 + u_y^2) + 1/4\rho(-u_x u_y - u_x^2 u_y + u_x u_y^2 + u_x^2 u_y^2). \tag{B.1i}$$

Appendix C. Multi-domain algorithm

The following algorithm describes the coupling between two grid resolution levels.

1. Initialize ρ and $\mathbf{u}$ on every domain and compute the equilibrium distributions f_i^{eq}.
2. Collide and Stream all distributions on the coarse grid. The coarse grid is now at time $t + \delta t_c$.
3. Collide and Stream once on the fine grid bringing it to time $t + \delta t_c/2$.
4. Perform a linear temporal interpolation of ρ_c, $\mathbf{u}_c$ and $f_{i,c}^{neq}$ at time $t + \delta t_c/2$ at the fine-coarse interface.
5. Spatially interpolate the values $\rho_c(t+\delta t_c/2)$, $\mathbf{u}_c(t+\delta t_c/2)$ and $f_{i,c}^{neq}(t+\delta t_c/2)$ at the fine nodes with no overlapping coarse nodes.

6. All populations at the fine grid boundaries are reconstructed following a convective scalling.
7. Collide and Stream once on the fine grid bringing it to time $t + \delta t_c$.
8. Spatially interpolate the values $\rho_c(t + \delta t_c)$, $\mathbf{u}_c(t + \delta t_c)$ and $f^{neq}_{i,c}(t + \delta t_c)$ as in step 5.
9. All populations at the fine grid boundaries are reconstructed following a convective scalling.
10. Save the equilibrium and non-equilibrium distributions $f^{eq}_{i,f}$, $f^{neq}_{i,f}$ at the coarse-fine interface.
11. Replace all the populations at the coarse-fine interface using filtering and scalling.
12. Proceed to the next time-step. Go to step 2.

If more resolution levels exist, a recursive algorithm based on the same principle of information exchange should be used. In this study, the computational domain is described with nine levels of refinement. A symmetric, cubic spline fitting is used for the spatial interpolation in steps 5 and 8 in order to eliminate any spatial asymmetries.

$$f(x) = \alpha_i + \beta_i x + \gamma_i x^2 + \delta_i x^3, \quad x_{i-1} \leq x_i \leq x_{i+1}. \tag{C.1}$$

The tridiagonal systems of equations are solved using the Thomas algorithm under the restrictions of nodal continuity of the function $f(x)$ and its first and second derivatives, as well as zero second derivative $f^{''}(x)$ at the end nodes. The reader should refer to Tölke and Krafczyk [73] for a different approach. The filtering process proposed by Pellerin *et al.* [74] is used in Step 11, where both the equilibrium and nominal distributions are filtered using the values at the nine neighbouring grid points.

$$\begin{aligned}\bar{f}_i(\mathbf{x}, t) = 0.25 f_i(\mathbf{x}, t) + 0.125(f_i(\mathbf{x} + \mathbf{e}_1, t) + f_i(\mathbf{x} + \mathbf{e}_2, t) + f_i(\mathbf{x} + \mathbf{e}_3, t) + f_i(\mathbf{x} + \mathbf{e}_4, t)) \\ + 0.0625(f_i(\mathbf{x} + \mathbf{e}_5, t) + f_i(\mathbf{x} + \mathbf{e}_6, t) + f_i(\mathbf{x} + \mathbf{e}_7, t) + f_i(\mathbf{x} + \mathbf{e}_8, t)),\end{aligned} \tag{C.2}$$

where the overbar denotes the filtered quantity. In this implementation, only the non-equilibrium part of the distributions that is proportional to the gradient of the velocity needs to be rescaled. Therefore, the scaling of the distributions in steps 6, 9 and 11 is described as

$$f_{i,c} = f^{eq}_i(\rho_f, \mathbf{u}_f) + \frac{2\omega_f}{\omega_c} \bar{f}^{neq}_{i,f}, \tag{C.3}$$

$$f_{i,f} = f^{eq,interpolated}_i(\rho_c, \mathbf{u}_c) + \frac{\omega_c}{2\omega_f} f^{neq,interpolated}_{i,c}. \tag{C.4}$$

What also differs from the work of Lagrava [45] is the equilibrium distribution function f^{eq} shown in Appendix B.

Appendix D. Normalised percentage error between periodic functions

Consider two periodic functions $f^{(1)}(t)$ and $f^{(2)}(t)$ and let $0.0T \leq t \leq 1.0T$, where T is the period of the oscillation. In order to quantify the observable percentage difference between $f^{(1)}(t)$ and $f^{(2)}(t)$ and avoid the regions where the values approximate the zero value, leading to big percentage errors, the following normalisation procedure is applied.

1. Compute the root mean square of $f^{(1)}(t)$ using

$$RMS_{f^1} = \sqrt{\frac{1}{N} \sum_1^N f^{(1)}(t)^2}, \tag{D.1}$$

   where N is the total number of discrete points.
2. Compute the distance D_{f^1} of $f^{(1)}(t)$ from its root mean square value for all N as $D_{f^1} = RMS_{f^1} - f^{(1)}(t)$.
3. Shift both functions $f^{(1)}(t)$ and $f^{(2)}(t)$ using the computed distance D_{f^1} as $f^{(1)}_{new}(t) = D_{f^1} + f^{(1)}(t)$ and $f^{(2)}_{new}(t) = D_{f^1} + f^{(2)}(t)$ respectively.
4. Compute the mean absolute percentage difference between $f^{(1)}_{new}(t)$ and $f^{(2)}_{new}(t)$ as

$$E = \frac{1}{N} \frac{\mid f^{(1)}_{new}(t) - f^{(2)}_{new}(t) \mid}{f^{(1)}_{new}(t)} \tag{D.2}$$

Acknowledgements

The first author wish to acknowledge funding from the Energy Technology Partnership (ETP) in support of his PhD studies [ETP125]. The ETP is a pooling exercise funded by the Scottish Funding Council and Scottish Enterprise. The authors also wish to thank Dr. Timm Krüger for his advice.

References

[1] S. Chapman and T. Cowling. *Mathematical Theory of Nonuniform Gases*. Cambridge University Press, 1964.

[2] C. Cercignani. *The Boltzmann Equation and Its Applications*, volume 67 of *Applied Mathematical Sciences*. Springer, 1988.

[3] D. A. Wolf-Gladrow. *Lattice-Gas Cellular Automata and Lattice Boltzmann Models: An Introduction*. Springer, 2004.

[4] Y. Sone. *Kinetic Theory and Fluid Dynamics*. Modeling and Simulation in Science, Engineering and Technology. Springer, 2002.

[5] M. Junk, A. Klar, and L.-S. Luo. Asymptotic analysis of the lattice Boltzmann equation. *J. Comput. Phys.*, 210(2):676–704, December 2005.

[6] P. Asinari. Generalized local equilibrium in the cascaded lattice Boltzmann method. *Phys. Rev. E*, 78(1), July 2008.

[7] H. Grad. On the kinetic theory of rarefied gases. *Comm. Pure Appl. Math*, 2(4):331–407, 1949.

[8] M. Geier, A. Greiner, and J. G. Korvink. A factorized central moment lattice Boltzmann method. *The European Physical Journal Special Topics*, 171(1):55–61, April 2009.

[9] Z.-G. Feng and E. E. Michaelides. The immersed boundary-lattice Boltzmann method for solving fluid - particles interaction problems. *J. Comput. Phys.*, 195(2):602–628, April 2004.

[10] T. Inamuro, K. Maeba, and F. Ogino. Flow between parallel walls containing the lines of neutrally buoyant circular cylinders. *Int. J. Multiphase Flow*, 26(12):1981 – 2004, 2000.

[11] M. Geier. *Ab initio derivation of the cascaded Lattice Boltzmann Automaton*. PhD dissertation, University of Freiburg - IMTEK, 2006.

[12] M. Geier, A. Greiner, and J. G. Korvink. Cascaded digital lattice Boltzmann automata for high Reynolds number flow. *Phys. Rev. E*, 73(6), June 2006.

[13] H. Chen, S. Chen, and W. H. Matthaeus. Recovery of the Navier-Stokes equations using a lattice-gas Boltzmann method. *Phys. Rev. A*, 45(8):R5339, 1992.

[14] Y. H. Qian, D. d'Humières, and P. Lallemand. Lattice BGK Models for Navier-Stokes Equation. *Europhys. Lett.*, 17(6):479, 1992.

[15] P. L. Bhatnagar, E. P. Gross, and M. Krook. A Model for Collision Processes in Gases. I. Small Amplitude Processes in Charged and Neutral One-Component Systems. *Physical Review*, 94(3):511, 1954.

[16] D. d'Humières. Generalized Lattice-Boltzmann Equations. In *Rarefied Gas Dynamics: Theory and Simulations, Progress in Astronautics and Aeronautics*, volume 159, pages 450–458. American Institute of Aeronautics and Astronautics, 1992.

[17] S. Ansumali and I. V. Karlin. Single relaxation time model for entropic lattice Boltzmann methods. *Phys. Rev. E*, 65(5), May 2002.

[18] S. Ansumali and I. V. Karlin. Stabilization of the lattice boltzmann method by the H theorem: A numerical test. *Phys. Rev. E*, 62:7999–8003, Dec 2000.

[19] C. S. Peskin. Numerical Analysis of Blood Flow in the Heart. *J. Comput. Phys.*, 25(3):220–252, 1977.

[20] C. S. Peskin. The immersed boundary method. *Acta Numerica*, 11, January 2002.

[21] R. Glowinski, T.W. Pan, T.I. Hesla, D.D. Joseph, and J. Périaux. A Fictitious Domain Approach to the Direct Numerical Simulation of Incompressible Viscous Flow past Moving Rigid Bodies: Application to Particulate Flow. *J. Comput. Phys.*, 169(2):363–426, May 2001.

[22] K. Höfler and S. Schwarzer. Navier-Stokes simulation with constraint forces: Finite-difference method for particle-laden flows and complex geometries. *Phys. Rev. E*, 61(6):7146, 2000.

[23] N. A. Patankar, P. Singh, D. D. Joseph, R. Glowinski, and T.-W. Pan. A new formulation of the distributed Lagrange multiplier/fictitious domain method for particulate flows. *Int. J. Multiphase Flow*, 26(9):1509–1524, 2000.

[24] K. Suzuki and T. Inamuro. Effect of internal mass in the simulation of a moving body by the immersed boundary method. *Comput. & Fluids*, 49(1):173 – 187, 2011.

[25] M.-C. Lai and C. S. Peskin. An Immersed Boundary Method with Formal Second-Order Accuracy and Reduced Numerical Viscosity. *J. Comput. Phys.*, 160(2):705–719, May 2000.

[26] J. J. Derksen A. ten Cate, C. H. Nieuwstad and H. E. A. Van den Akker. Particle imaging velocimetry experiments and lattice-Boltzmann simulations on a single sphere settling under gravity. *Physics of Fluids*, 14(4), 2002.

[27] M. Uhlmann. An immersed boundary method with direct forcing for the simulation of particulate flows. *J. Comput. Phys.*, 209(2):448 – 476, 2005.

[28] Z.-G. Feng and E. E. Michaelides. Robust treatment of no-slip boundary condition and velocity updating for the lattice-Boltzmann simulation of particulate flows. *Comput. & Fluids*, 38(2):370 – 381, 2009.

[29] A. J. C. Ladd and R. Verberg. Lattice-boltzmann simulations of particle-fluid suspensions. *Journal of Statistical Physics*, 104(5):1191–1251, Sep 2001.

[30] L. Shen, E.-S. Chan, and P. Lin. Calculation of hydrodynamic forces acting on a submerged moving object using immersed boundary method. *Comput. & Fluids*, 38(3):691 – 702, 2009.

[31] E. Balaras. Modeling complex boundaries using an external force field on fixed cartesian grids in large-eddy simulations. *Comput. & Fluids*, 33(3):375 – 404, 2004.

[32] A. Dupuis, P. Chatelain, and P. Koumoutsakos. An immersed boundary-lattice-Boltzmann method for the simulation of the flow past an impulsively started cylinder. *J. Comput. Phys.*, 227(9):4486–4498, April 2008.

[33] X.D. Niu, C. Shu, Y.T. Chew, and Y. Peng. A momentum exchange-based immersed boundary-lattice Boltzmann method for simulating incompressible viscous flows. *Phys. Lett. A*, 354(3):173–182, May 2006.

[34] S. K. Kang and Y. A. Hassan. A comparative study of direct-forcing immersed boundary-lattice Boltzmann methods for stationary complex boundaries. *Int. J. Numer. Meth. Fluids*, 66(9):1132–1158, July 2011.

[35] T. Inamuro. Lattice Boltzmann methods for moving boundary flows. *Fluid Dyn. Res.*, 44(2):024001, April 2012.

[36] C. Zhang, Y. Cheng, L. Zhu, and J. Wu. Accuracy improvement of the immersed boundary-lattice Boltzmann coupling scheme by iterative force correction. *Comput. & Fluids*, 124:246–260, January 2016.

[37] Y. Cheng and J. Li. Introducing unsteady non-uniform source terms into the lattice Boltzmann model. *Int. J. Num. Meth. Fluids*, 56(6):629–641, February 2008.

[38] J. Wu and C. Shu. Implicit velocity correction-based immersed boundary-lattice Boltzmann method and its applications. *J. Comput. Phys.*, 228(6):1963–1979, April 2009.

[39] Z. Guo, C. Zheng, and B. Shi. Discrete lattice effects on the forcing term in the lattice Boltzmann method. *Phys. Rev. E*, 65(4), April 2002.

[40] E. J. Falagkaris, D. M. Ingram, I. M. Viola, and K. Markakis. PROTEUS: A coupled iterative force-correction immersed-boundary multi-domain cascaded lattice boltzmann solver. *Comput. Math. Appl.*

[41] D. Yu, R. Mei, L.-S. Luo, and W. Shyy. Viscous flow computations with the method of lattice Boltzmann equation. *Progress in Aerospace Sciences*, 39(5):329–367, July 2003.

[42] K. N. Premnath and S. Banerjee. Incorporating forcing terms in cascaded lattice Boltzmann approach by method of central moments. *Phys. Rev. E*, 80(3):036702, 2009.

[43] X. Yang, X. Zhang, Z. Li, and G.-W. He. A smoothing technique for discrete delta functions with application to immersed boundary method in moving boundary simulations. *J. Comput. Phys.*, 228(20):7821–7836, November 2009.

[44] Y. Cheng, L. Zhu, and C. Zhang. Numerical Study of Stability and Accuracy of the Immersed Boundary Method Coupled to the Lattice Boltzmann BGK Model. *Commun. Comput. Phys.*, 16(01):136–168, July 2014.

[45] D. Lagrava, O. Malaspinas, J. Latt, and B. Chopard. Advances in multi-domain lattice Boltzmann grid refinement. *J. Comput. Phys.*, 231(14):4808–4822, May 2012.

[46] M. Rohde, D. Kandhai, J. J. Derksen, and H. E. A. van den Akker. A generic, mass conservative local grid refinement technique for lattice-Boltzmann schemes. *Int. J. Numer. Meth. Fluids*, 51(4):439–468, June 2006.

[47] A. Dupuis and B. Chopard. Theory and applications of an alternative lattice Boltzmann grid refinement algorithm. *Phys. Rev. E*, 67(6), June 2003.

[48] M. Schönherr, K. Kucher, M. Geier, M. Stiebler, S. Freudiger, and M. Krafczyk. Multi-thread implementations of the lattice boltzmann method on non-uniform grids for CPUs and GPUs. *Comput. Math. Appl.*, 61(12):3730 – 3743, 2011.

[49] O. Filippova and D. Hänel. Grid Refinement for Lattice-BGK Models. *J. Comput. Phys.*, 147(1):219 – 228, 1998.

[50] J. Latt and B. Chopard. Lattice Boltzmann method with regularized pre-collision distribution functions. *Math. Comput. Simulation*, 72(2):165–168, 2006.

[51] Q. Zou and X. He. On pressure and velocity boundary conditions for the lattice Boltzmann BGK model. *Phys. Fluids*, 9(6):1591–1598, 1997.

[52] M. Geier, M. Schönherr, A. Pasquali, and M. Krafczyk. The cumulant lattice Boltzmann equation in three dimensions: Theory and validation. *Comput. Math. Appl.*, 70(4):507–547, August 2015.

[53] H. Xu and P. Sagaut. Analysis of the absorbing layers for the weakly-compressible lattice Boltzmann methods. *J. Comput. Phys.*, 245:14–42, July 2013.

[54] H. Dütsch, F. Durst, S. Becker, and H. Lienhart. Low-Reynolds-number flow around an oscillating circular cylinder at low KeuleganCarpenter numbers. *J. Fluid Mech.*, 360:249271, 1998.

[55] C.-C. Liao, Y.-W. Chang, C.-A. Lin, and J.M. McDonough. Simulating flows with moving rigid boundary using immersed-boundary method. *Comput. & Fluids*, 39(1):152 – 167, 2010.

[56] D. Kim and H. Choi. Immersed boundary method for flow around an arbitrarily moving body. *J. Comput. Phys.*, 212(2):662 – 680, 2006.

[57] J.-I. Choi, R. C. Oberoi, J. R. Edwards, and J. A. Rosati. An immersed boundary method for complex incompressible flows. *J. Comput. Phys.*, 224(2):757 – 784, 2007.

[58] J.R. Morison, J.W. Johnson, and S.A. Schaaf. The Force Exerted by Surface Waves on Piles. *J. Petrol. Technol.*, 2:149–154, 1950.

[59] B. Uzunoğlu, M. Tan, and W. G. Price. Low-Reynolds-number flow around an oscillating circular cylinder using a cell viscousboundary element method. *Int. J. Numer. Meth. in Engng*, 50(10):2317–2338, 2001.

[60] R. Yuan, C. Zhong, and He Zhang. An immersed-boundary method based on the gas kinetic bgk scheme for incompressible viscous flow. *J. Comput. Phys.*, 296:184 – 208, 2015.

[61] R. Godoy-Diana, J.-L. Aider, and J. E. Wesfreid. Transitions in the wake of a flapping foil. *Phys. Rev. E*, 77:016308, Jan 2008.

[62] R. Godoy-Diana, C. Marais, J.-L. Aider, and J.-E. Wesfreid. A model for the symmetry breaking of the reverse Bénardvon Kármán vortex street produced by a flapping foil. *J. Fluid Mech.*, 622:2332, 2009.

[63] M. Visbal. High-Fidelity simulation of transitional flows past a plunging airfoil. In *47th AIAA Aerospace Sciences Meeting including The New Horizons Forum and Aerospace Exposition*. AIAA, 2009.

[64] R. E. Radespiel, J. Windte, and U. Scholz. Numerical and Experimental Flow Analysis of Moving Airfoils with Laminar Separation Bubbles. *AIAA Journal*, 45(6):1346–1356, 2007.

[65] W. Yuan, M. Khalid, J. Windte, U. Scholz, and R. Radespiel. *An Investigation of Low-Reynolds-Number Flows Past Airfoils*. AIAA, 2017/06/25 2005.

[66] M. Galbraith and M. Visbal. *Implicit Large Eddy Simulation of Low-Reynolds-Number Transitional Flow Past the SD7003 Airfoil*. AIAA, 2017/06/25 2010.

[67] G. McGowan, A. Gopalarathnam, V. Ol. Michael, J. Edwards, and D. Fredberg. Computation vs. Experiment for High-Frequency Low-Reynolds Number Airfoil Pitch and Plunge. In *46th AIAA Aerospace Sciences Meeting and Exhibit*. AIAA, 2008.

[68] Fung Y. C. *An Introduction to the Theory of Aeroelasticity*. Dover, 1993.

[69] Ismail H. Tuncer and Mustafa Kaya. Thrust generation caused by flapping airfoils in a biplane configuration. *Journal of Aircraft*, 40(3):509–515, 2017/07/03 2003.

[70] M.M. Murray and L.E. Howle. Spring stiffness influence on an oscillating propulsor. *Journal of Fluids and Structures*, 17(7):915 – 926, 2003.

[71] J.-M. Miao and M.-H. Ho. Effect of flexure on aerodynamic propulsive efficiency of flapping flexible airfoil. *Journal of Fluids and Structures*, 22(3):401 – 419, 2006.

[72] D.A. Read, F.S. Hover, and M.S. Triantafyllou. Forces on oscillating foils for propulsion and maneuvering. *Journal of Fluids and Structures*, 17(1):163 – 183, 2003.

[73] J. Tölke and M. Krafczyk. Second order interpolation of the flow field in the lattice boltzmann method. *Comput. Math. Appl.*, 58(5):898 – 902, 2009. Mesoscopic Methods in Engineering and Science.

[74] N. Pellerin, S. Leclaire, and M. Reggio. An implementation of the Spalart - Allmaras turbulence model in a multi-domain lattice Boltzmann method for solving turbulent airfoil flows. *Comput. Math. Appl.*, 70(12):3001–3018, December 2015.